University of Nebraska - Lincoln
DigitalCommons@University of Nebraska - Lincoln

Publications, Agencies and Staff of the U.S. Department of Commerce

U.S. Department of Commerce

2016

Precipitation and Growth of Barite within Hydrothermal Vent Deposits from the Endeavour Segment, Juan de Fuca Ridge

John William Jamieson
GEOMAR – Helmholtz Centre for Ocean Research Kiel, jjamieson@geomar.de

Mark D. Hannington
GEOMAR – Helmholtz Centre for Ocean Research Kiel, mhannington@geomar.de

Margaret K. Tivey
Woods Hole Oceanographic Institution, mktivey@whoi.edu

Thor Hansteen
GEOMAR – Helmholtz Centre for Ocean Research Kiel, thansteen@geomar.de

Nicole M.-B. Williamson
University of Ottawa, nmb.williamson@gmail.com

See next page for additional authors

Follow this and additional works at: http://digitalcommons.unl.edu/usdeptcommercepub


Part of the Geochemistry Commons, Mineral Physics Commons, and the Tectonics and Structure Commons

Jamieson, John William; Hannington, Mark D.; Tivey, Margaret K.; Hansteen, Thor; Williamson, Nicole M.-B.; Stewart, Margaret; Fietzke, Jan; Butterfield, David; Frische, Matthias; Allen, Leigh; Cousens, Brian; and Langer, Julia, "Precipitation and Growth of Barite within Hydrothermal Vent Deposits from the Endeavour Segment, Juan de Fuca Ridge" (2016). *Publications, Agencies and Staff of the U.S. Department of Commerce*. 541.
http://digitalcommons.unl.edu/usdeptcommercepub/541

This Article is brought to you for free and open access by the U.S. Department of Commerce at DigitalCommons@University of Nebraska - Lincoln. It has been accepted for inclusion in Publications, Agencies and Staff of the U.S. Department of Commerce by an authorized administrator of DigitalCommons@University of Nebraska - Lincoln.

Authors
John William Jamieson, Mark D. Hannington, Margaret K. Tivey, Thor Hansteen, Nicole M.-B. Williamson, Margaret Stewart, Jan Fietzke, David Butterfield, Matthias Frische, Leigh Allen, Brian Cousens, and Julia Langer

This article is available at DigitalCommons@University of Nebraska - Lincoln: http://digitalcommons.unl.edu/usdeptcommercepub/541

Available online at www.sciencedirect.com

ScienceDirect

Geochimica et Cosmochimica Acta 173 (2016) 64–85

Geochimica et Cosmochimica Acta

www.elsevier.com/locate/gca

Precipitation and growth of barite within hydrothermal vent deposits from the Endeavour Segment, Juan de Fuca Ridge

John William Jamieson [a,b,*], Mark D. Hannington [a,b], Margaret K. Tivey [c], Thor Hansteen [a], Nicole M.-B. Williamson [b], Margaret Stewart [d], Jan Fietzke [a], David Butterfield [e], Matthias Frische [a], Leigh Allen [b], Brian Cousens [d], Julia Langer [a]

[a] GEOMAR – Helmholtz Centre for Ocean Research Kiel, Wischhofstr. 1-3, 24148 Kiel, Germany
[b] University of Ottawa, FSS Hall, 120 University, Ottawa, ON K1N 6N5, Canada
[c] Woods Hole Oceanographic Institution, 266 Woods Hole Road, Woods Hole, MA 02543-1050, USA
[d] Carleton University, 1125 Colonel By Drive, Ottawa, ON K1S 5B6, Canada
[e] University of Washington and NOAA/PMEL, 7600 Sand Point Way NE, Seattle, WA 98115, USA

Received 3 July 2015; accepted in revised form 21 October 2015; Available online 27 October 2015

Abstract

Hydrothermal vent deposits form on the seafloor as a result of cooling and mixing of hot hydrothermal fluids with cold seawater. Amongst the major sulfide and sulfate minerals that are preserved at vent sites, barite ($BaSO_4$) is unique because it requires the direct mixing of Ba-rich hydrothermal fluid with sulfate-rich seawater in order for precipitation to occur. Because of its extremely low solubility, barite crystals preserve geochemical fingerprints associated with conditions of formation. Here, we present data from petrographic and geochemical analyses of hydrothermal barite from the Endeavour Segment of the Juan de Fuca Ridge, northeast Pacific Ocean, in order to determine the physical and chemical conditions under which barite precipitates within seafloor hydrothermal vent systems. Petrographic analyses of 22 barite-rich samples show a range of barite crystal morphologies: dendritic and acicular barite forms near the exterior vent walls, whereas larger bladed and tabular crystals occur within the interior of chimneys. A two component mixing model based on Sr concentrations and $^{87}Sr/^{86}Sr$ of both seawater and hydrothermal fluid, combined with $^{87}Sr/^{86}Sr$ data from whole rock and laser-ablation ICP-MS analyses of barite crystals indicate that barite precipitates from mixtures containing as low as 17% and as high as 88% hydrothermal fluid component, relative to seawater. Geochemical modelling of the relationship between aqueous species concentrations and degree of fluid mixing indicates that Ba^{2+} availability is the dominant control on mineral saturation. Observations combined with model results support that dendritic barite forms from fluids of less than 40% hydrothermal component and with a saturation index greater than ~0.6, whereas more euhedral crystals form at lower levels of supersaturation associated with greater contributions of hydrothermal fluid. Fluid inclusions within barite indicate formation temperatures of between ~120 °C and 240 °C during barite crystallization. The comparison of fluid inclusion formation temperatures to modelled mixing temperatures indicates that conductive cooling of the vent fluid accounts for 60–120 °C reduction in fluid temperature. Strontium zonation within individual barite crystals records fluctuations in the amount of conductive cooling within chimney walls that may result

* Corresponding author at: GEOMAR – Helmholtz Centre for Ocean Research Kiel, Wischhofstr. 1-3, 24148 Kiel, Germany.
E-mail addresses: jjamieson@geomar.de (J.W. Jamieson), mhannington@geomar.de (M.D. Hannington), mktivey@whoi.edu (M.K. Tivey), thansteen@geomar.de (T. Hansteen), nmb.williamson@gmail.com (N.M.-B. Williamson), meg.engelbert@gmail.com (M. Stewart), jfietzke@geomar.de (J. Fietzke), david.a.butterfield@noaa.gov (D. Butterfield), mfrische@geomar.de (M. Frische), Leigh.alle@gmail.com (L. Allen), brian.cousens@carleton.ca (B. Cousens), j.-langer@outlook.com (J. Langer).

http://dx.doi.org/10.1016/j.gca.2015.10.021
0016-7037/© 2015 Elsevier Ltd. All rights reserved.

This document is a U.S. government work and is not subject to copyright in the United States.

from cyclical oscillations in hydrothermal fluid flux. Barite chemistry and morphology can be used as a reliable indicator for past conditions of mineralization within both extinct seafloor hydrothermal deposits and ancient land-based volcanogenic massive sulfide deposits.
© 2015 Elsevier Ltd. All rights reserved.

1. INTRODUCTION

Heat from shallow magmatic activity drives the circulation of seawater through oceanic crust along volcanically-active mid-ocean ridges, arcs, and back-arc basins (Baker et al., 1995; Hannington et al., 2005). As fluids circulate, they are heated, and react with the surrounding rock, resulting in leaching and transport of dissolved chemical constituents from the underlying substrate to the seafloor. Hydrothermal chimneys and mounds form on the seafloor at sites where the high temperature, focused hydrothermal fluid discharges, and where mineral precipitation is driven by the mixing of the hot vent fluid with local cold seawater (Von Damm, 1990; Hannington et al., 1995).

The composition of the substrate is a major control on both vent fluid composition and the mineralogy of the hydrothermal deposits that form on the seafloor (e.g., Von Damm, 1990). The primary minerals that typically make up vent edifices are sulfides such as pyrite, sphalerite, chalcopyrite, pyrrhotite, sulfates such as barite and anhydrite, and amorphous silica. These minerals precipitate either from dissolved constituents within the hydrothermal fluids (e.g., pyrite precipitated from dissolved Fe^{2+} and H_2S or HS^-), from dissolved constituents within locally heated seawater (e.g., anhydrite precipitated from dissolve Ca^{2+} and SO_4^{2-}), or from dissolved constituents within both fluids (e.g., barite and anhydrite precipitated from Ba^{2+} and Ca^{2+}, respectively, in hydrothermal fluid that has mixed with SO_4^{2-}-rich seawater) (Von Damm, 1990; Tivey et al., 1999; Hannington et al., 2005; Humphris and Bach, 2005). Mineral precipitation is driven mainly by the changes in temperature, pH, fO_2, and concentration of dissolved ions that accompany the mixing of hot hydrothermal fluid and cold seawater, although fluid temperature can also be affected by conductive cooling and heating (Tivey and McDuff, 1990; Hannington et al., 1995; Tivey, 1995; Tivey et al., 1999; Ruiz-Agudo et al., 2015). The occurrence of specific minerals or mineral assemblages within a chimney thus largely reflects the physicochemical properties of the local fluid at the time of precipitation. High-temperature minerals (minerals that precipitate at temperatures above ~300 °C, such as chalcopyrite, pyrrhotite, wurtzite) precipitate primarily along inner fluid conduits, where there is limited infiltration of cold seawater (Hannington et al., 1995). The porous outer chimney walls typically contain a lower-temperature (<~300 °C) suite of minerals (e.g., sphalerite, barite, and amorphous silica) that precipitate as a result of a higher degree of mixing with seawater, and/or conductive cooling of the hydrothermal fluid (Hannington et al., 1995; Tivey et al., 1999).

Barite and other low-temperature minerals dominate the early and late growth stages of a hydrothermal chimney that are characterized by lower hydrothermal fluxes and fluid temperatures (Tivey et al., 1990; Hannington et al., 1995). However, precipitation of these low-temperature minerals will still occur within chimneys formed from high-temperature venting, often in the exterior walls of a chimney where extensive mixing with seawater occurs (Hannington and Scott, 1988; Hannington et al., 1991). Barite is especially important as a key structural component to hydrothermal edifices on the seafloor, and its occurrence and abundance can affect hydrothermal deposit morphology, the style of venting and chimney growth, and the retention of metals within a deposit (Tivey and Delaney, 1986; Hannington et al., 1995). Precipitation of barite occurs when the product of the concentrations of Ba^{2+} (from the hydrothermal fluid) and SO_4^{2-} (from seawater) exceed the solubility constant of the mixed fluid (Blount, 1977). Endmember concentrations of Ba in hydrothermal fluids from Main Endeavour Field have been measured at concentrations of up to 31 μmol/kg (Seyfried et al., 2003), indicating significant enrichment of Ba relative to ambient seawater (0.1 μmol/kg) resulting from leaching of Ba during hydrothermal alteration of basalt (Chan et al., 1976; Kim and McMurtry, 1991). Modern seawater contains ~28 mmol/kg of dissolved sulfate, whereas sulfate concentrations in endmember hydrothermal fluids are generally near zero as a result of precipitation of anhydrite within the crust and the thermo-chemical reduction of remaining sulfate during high-temperature reactions with basalt (Seyfried et al., 2003; Halevy et al., 2012). In contrast to anhydrite, which is unstable and will dissolve at ambient seafloor temperatures, barite has extremely low solubility in seawater and behaves as a closed system under typical oxic seafloor conditions, and is not prone to diagenetic alteration (Averyt and Paytan, 2003, and references therein; Widanagamage et al., 2014). Barite can thus preserve geochemical and morphological features associated with initial conditions of crystallization long after hydrothermal venting has ceased, and the occurrence, and crystallographic and geochemical properties of barite can provide insights into fluid mixing and the physicochemical conditions that drive mineral precipitation within the walls of hydrothermal chimneys. Barite is also the primary host in hydrothermal deposits for Ra, a radiogenic element that also has a similar ionic charge and radius to Ba. The closed system behavior of barite allows for the decay of ^{226}Ra (half-life of 1600 years) within the crystals to be used to determine absolute ages of chimneys (Ditchburn et al., 2004; de Ronde et al., 2005; Ditchburn et al., 2012; Jamieson et al., 2013a).

Strontium is an abundant dissolved cation in both seawater and hydrothermal fluids, with seawater and Endeavour hydrothermal concentrations of ~87 μmol/kg and

~135 μmol/kg, respectively (Turekian, 1968; Butterfield et al., 1994; Seyfried et al., 2003). With a similar ionic charge and radius to Ba, Sr is a common trace substitution in barite. At the same time, both seawater and hydrothermal fluid at Endeavour have very different Sr-isotope ($^{87}Sr/^{86}Sr$) ratios. These ratios can be compared to the ratios measured in barite crystals to determine the relative proportion of seawater and hydrothermal fluid that make up the fluid mixture from which barite precipitated. A similar approach has been used to investigate the precipitation of anhydrite within the main active mound at the TAG hydrothermal field on the Mid-Atlantic Ridge (Mills et al., 1998; Teagle et al., 1998) and the 21° North site on the East Pacific Rise (Albarede et al., 1981). However, there are few reports of similar studies for hydrothermal barite (Kusakabe et al., 1990).

In this study, we present data on the morphology, trace element distribution, Sr-isotope composition and fluid inclusion analysis of barite collected from active and inactive hydrothermal chimneys on the Endeavour Segment of the Juan de Fuca Ridge. The integrated analysis of these multiple datasets provides constraints on the physical and chemical controls associated with fluid mixing for barite precipitation within hydrothermal chimney walls. Results of geochemical modeling are used to link the qualitative petrographic observations of barite occurrence within the vent chimneys to the quantitative constraints on fluid mixing and the physicochemical conditions of barite precipitation. This information can be used to infer the formation temperatures and fluid chemistry of inactive chimneys, provide insights into the role of fluid mixing within chimneys for the precipitation of other chimney-forming minerals, and evaluate the locations favourable for microbial habitat within chimneys.

2. GEOLOGICAL SETTING

The Endeavour Segment is a 90 km-long section of the Juan de Fuca mid-ocean ridge, which is spreading at an average full-spreading rate of ~6 cm/yr (Fig. 1) (Riddihough, 1984; Goldstein et al., 1991). The segment, shown in red in the inset of Fig. 1, is bound to the south by the Cobb Offset and the Cobb overlapping spreading center (OSC) and to the north by the Endeavour Offset and the Endeavour OSC. The Cobb Offset represents a major geochemical division in the Juan de Fuca Ridge, with normal mid-ocean ridge basalt (N-MORB) dominating the oceanic crust south of the offset and enriched-MORB (E-MORB) dominating oceanic crust north of the offset (Karsten et al., 1990). The occurrence of E-MORB at Endeavour has been attributed to a heterogeneous mantle source of both enriched and depleted upper mantle with the enriched component of the mantle source exhibiting enhanced melting relative to the depleted mantle source (Cousens, 2010).

The Endeavour Segment ranges in depth from 2050 meters below sea level (mbsl) at a central bathymetric high to >2700 mbsl towards the south end of the segment (Fig. 1) (Delaney et al., 1992). Active hydrothermal venting is focused within a 15 km-long central axial valley that bisects the central volcanic high (Kelley et al., 2012). Within the axial valley are five major hydrothermal vent fields (Sasquatch, Salty Dawg, High Rise, Main Endeavour Field, Mothra), with several smaller vent fields and diffusely venting areas, making the Endeavour Segment one of the most active hydrothermal areas on the mid-ocean ridge system (Fig. 1) (Kelley et al., 2012). Numerous inactive or extinct sulfide edifices occur on the axial valley floor outside of the active vent fields (Clague et al., 2008; Jamieson et al., 2014). Hydrothermal activity has been ongoing within the axial valley for at least the past ~3000 years (Jamieson et al., 2013a).

The sulfide edifices at Endeavour are typically steep-sided, often reaching heights of greater than 20 metres above the seafloor, with fluid venting temperatures that range from <10 °C up to ~375 °C (Delaney et al., 1992; Robigou et al., 1993; Butterfield et al., 1994; Glickson et al., 2006; Kelley et al., 2012). The edifices are rich in barite relative to typical mid-ocean ridge deposits. The high abundance of barite has been linked to the high Ba content of the underlying E-MORB crust (Karsten et al., 1990; Tivey et al., 1999) and/or the presence of buried sediments that have modified the chemistry of the hydrothermal fluids prior to venting (Lilley et al., 1993; Butterfield et al., 1994; You et al., 1994; Proskurowski et al., 2004; Yao et al., 2009).

Vent fluid chemistry within the Main Endeavour Field has been shown to be remarkably stable from year to year (Butterfield et al., 1994). However, significant changes in fluid composition over short periods have been linked to local seismic events (Seyfried et al., 2003). Factors such as low chlorinity relative to seawater, and short-lived venting of high-temperature, volatile-rich fluids suggest that subsurface phase separation is an ongoing process (Butterfield et al., 1994; Larson et al., 2009; Kelley et al., 2012).

3. ANALYTICAL METHODS

Barite-rich samples for this study were collected from active and inactive hydrothermal structures using remotely-operated vehicles (ROVs) and occupied submersible during several research cruises to the Endeavour Segment between 1984 and 2011 (Delaney et al., 1992; Robigou et al., 1993; Tivey et al., 1999; Kelley et al., 2001; Kristall et al., 2006; Kelley et al., 2012; Glickson et al., 2006; Glickson et al., 2007; Jamieson et al., 2013a). Samples are generally fist-sized, and therefore their contained mineralogy and bulk chemistry may not reflect that of the entire vent from which they were sampled. Thin sections and doubly-polished thick sections (80 μm) were prepared for petrographic and fluid inclusion analysis, respectively, by first impregnating the samples in epoxy due to their fragile nature, and then cutting and polishing each sample. Thin sections were examined using both reflected and transmitted light modes with an Olympus BX 51 polarizing microscope with an attached Olympus DP71 digital camera.

Two samples – ALV2464-R4 and ALV2467-R2 – were selected for detailed analysis of barite growth due to their large (>0.5 mm), euhedral zoned tabular barite crystals

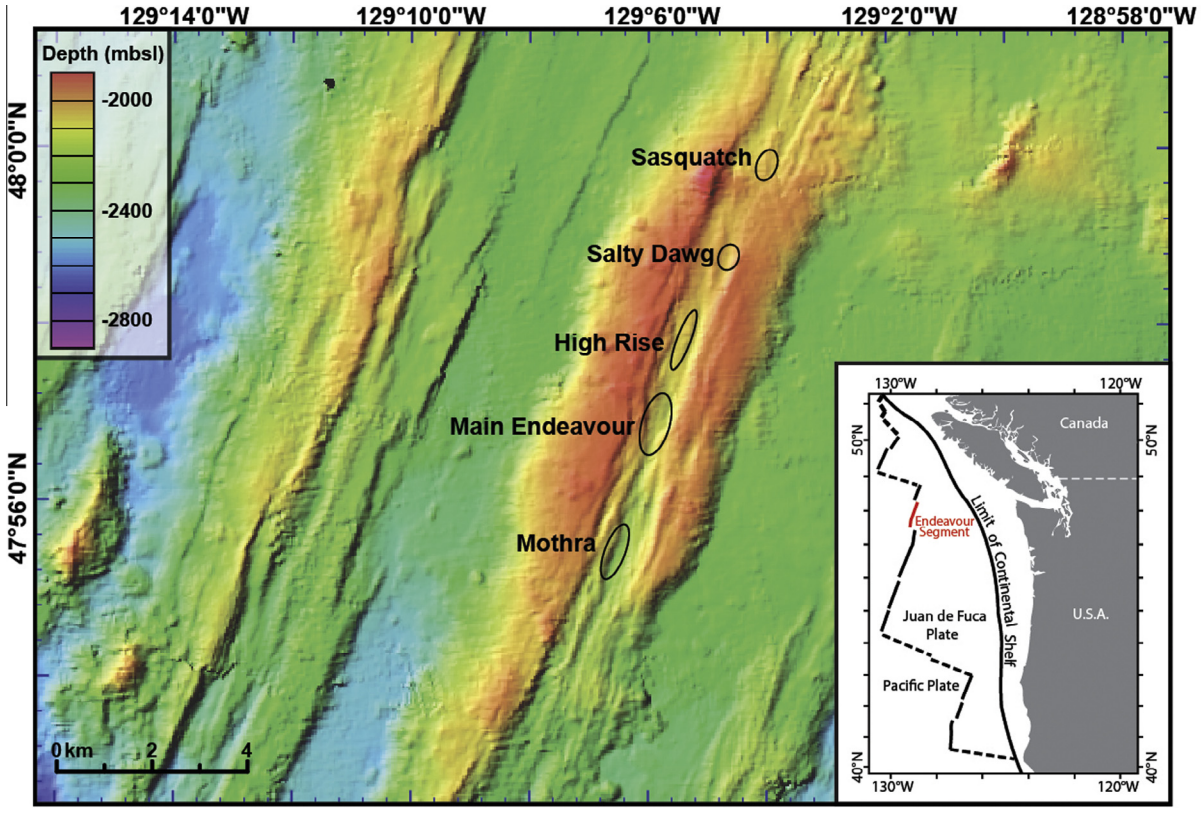

Fig. 1. Bathymetric map of the Endeavour Segment, with the locations of the major active vent fields. Inset map shows the location of the Endeavour Segment on the Juan de Fuca Ridge. Bathymetric data collected using hull-mounted EM300 multibeam system on the *R/V Thomas G. Thompson* (TN146) (Kelley, 2015; www.geomapapp.org).

(Fig. 2). Sample ALV2464-R4 is barite-rich and sulfur-poor, and was collected from the side of an old, Mn-coated 1.5 m tall, 1 m wide extinct spire within the High Rise vent field. ALV2467-R2 was collected from a tall, thin extinct spire north of the Main Endeavour field.

3.1. Geochemistry

Concentrations of Ba, Ca and Sr within bulk samples were determined at ActLabs, in Ontario, Canada, using a combination of fusion followed by multi-acid dissolution and inductively coupled mass spectrometry, instrumental neutron activation analysis (for Ba), and inductively-coupled plasma emission spectroscopy (for Ca and Sr). The reporting uncertainties are <10% over the range of measured concentrations.

3.2. Electron microprobe analysis

Concentrations of Sr, Ba, Ca and SO_4 within individual barite crystals were determined by electron microprobe analysis (EMPA). Barites from seven carbon-coated thin-sections were analyzed using an automated 4-spectrometer Cameca Camebax MBX electron microprobe at Carleton University, using both energy-dispersive and wavelength-dispersive analytical modes, with an accelerating voltage of 15 keV and a 20 nA beam current. Samples were selected in order to maximize the variability in sample bulk Sr/Ba and barite crystal morphology. Analyses for Fe, Cl, Cu and Zn returned concentrations below analytical detection limits (<0.01 wt.%).

3.3. Fluid Sr-isotope analysis

Thirty-one hydrothermal fluid samples for Sr isotope analysis were collected in 1995 and 2003 from high-temperature vents along the Endeavour Segment using titanium syringe major samplers and the Hydrothermal Fluid and Particle Sampler (Butterfield et al., 2004). Sub-samples for Sr isotope analysis were stored in acid-cleaned HDPE bottles and acidified with ultra-pure HCl to pH <2. Strontium isotope compositions of fluids were analyzed by thermal ionization mass spectrometry at the University of Washington with methods described by Nelson (1995). Magnesium concentration was determined by ion chromatography (precision 1%). Strontium concentration in vent fluids was determined by atomic absorption spectrophotometry (precision 4%).

3.4. Whole-rock Sr-isotope analysis

The bulk strontium isotope ($^{87}Sr/^{86}Sr$) composition of 16 barite-rich samples was determined using thermal ionization mass spectrometry. For each analysis, approximately 50 mg of crushed sample was leached in ~2 mL of 7 M HNO3 on a 100 °C hot plate in order to dissolve the sulfide

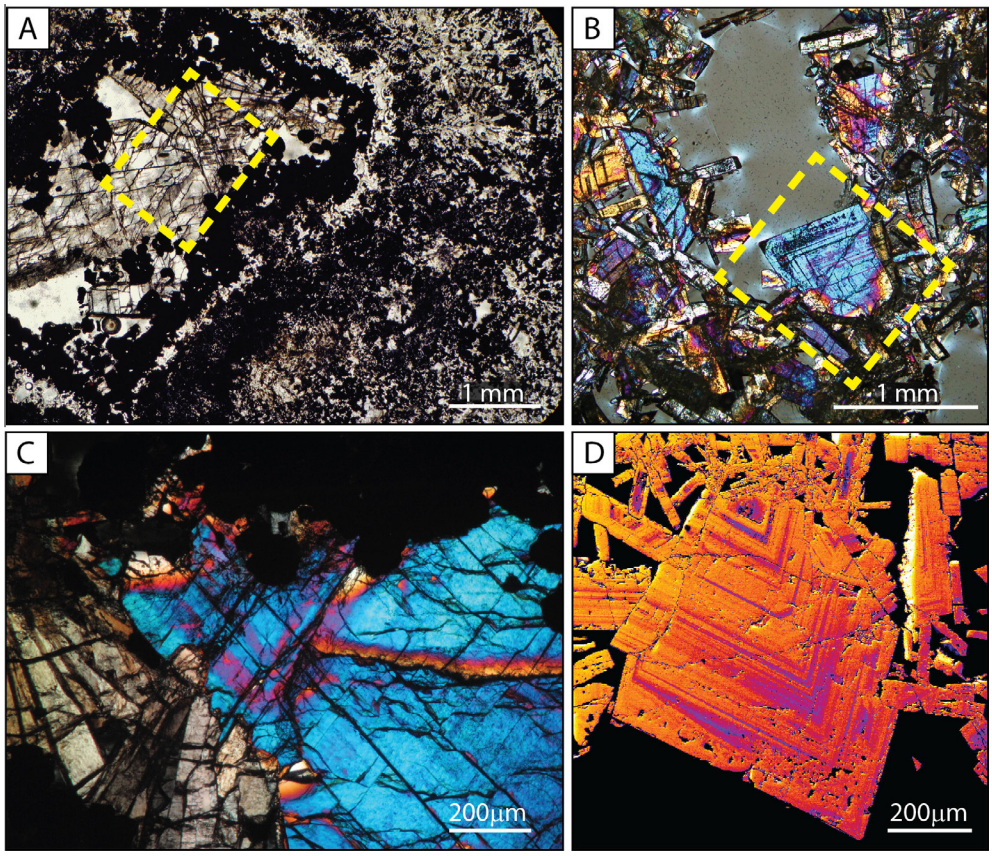

Fig. 2. (A) Plane-polarized photomicrograph of ALV2467-R2, with a fluid conduit infilled by tabular barite. The conduit is lined with dark-red to opaque rounded sphalerite grains. The surrounding matrix consists of bladed barite, fine sphalerite with minor pyrite and late-stage amorphous silica. (B) Cross-polarized photomicrograph of ALV2464-R4, showing tabular and bladed barite crystals that grew into open pore space. Yellow dashed boxes in A and B show location of detailed images in C and D, respectively. (C) Cross-polarized photomicrograph of tabular barite crystal from A. The magenta colour within the blue crystal indicates Sr-rich growth zones. (D) Coloured electron microprobe backscatter image of barite crystal from B. Again, magenta colours indicate Sr-rich growth zones. Some interference colours of barite in cross-polarized images in this figure, as well as Fig. 3, appear as second-order colours due to the thin sections have a thickness of slightly greater than 30 µm. (For interpretation of the references to colour in this figure legend, the reader is referred to the web version of this article.)

minerals. This process was repeated three times in order to ensure complete dissolution of sulfides. The remaining barite crystals were immersed in 6 M HCl and left covered on a 100 °C hot plate for three days. The solution was then removed by pipette and the samples were left to dry down overnight. Finally, 1.5 mL of 2.5 M HCl was added to each solution and the samples were left covered for two days. The solutions containing the dissolved barite were run through Sr resin columns to isolate the Sr. The resulting samples were analyzed using a ThermoFinnigan TRITON thermal ionization multi-collector mass spectrometer at Carleton University. Samples underwent ~100 analyses at 1200–1406 °C with a baseline measurement taken after every 10 analyses.

3.5. In situ laser ablation analysis

Concentrations of a suite of 61 elements from Sr-rich and Sr-poor zones of a single crystal were measured using a 193 nm Excimer laser ablation system (GeoLasPro, Coherent) coupled to a double-focusing, high-resolution magnetic sector mass spectrometer (AttoM, Nu Instruments) at GEOMAR (Fietzke and Frische, 2016). Individual analyses on the crystal surface consisted of continuous sampling along 100 µm rasters parallel to the mineral zonation at a scan rate of 3 µm/s, with a 32 µm beam width and a fluence of 2 J/cm^2 at a repetition rate of 10 Hz. Ablation sites were chosen in order to avoid fractures or areas with abundant fluid inclusions. Two standard reference glasses (NIST SRM 612 and 610) and a synthetic sulfide standard (PGE_Ni7b) were used for calibration.

A New Wave UP193 laser, attached to an AXIOM multi-collector inductively-coupled plasma mass spectrometer, also at GEOMAR, was used to measure the $^{87}Sr/^{86}Sr$ composition of individual zones within single barite crystals from two samples, including the same crystal analyzed for trace element abundances. Analyses and data reduction using a LRS (linear regression slope) method followed the approach described by Fietzke et al. (2008).

Single analyses on the crystal surfaces consisted of 100 µm line scan ablations parallel to the Sr zonation using a spot size of 25 µm, fluence of 2 J/cm^2 and repetition rate of 10 Hz at a 3 µm/s scan speed. Precision and accuracy of the measurements was evaluated by repeat duplicate analysis of

a modern marine carbonate reference standard after every fifth analysis. See Supplementary information for further analytical details.

3.6. Microthermometry

For microthermometry measurements, samples were prepared as ~50 μm-thick doubly polished sections mounted with acetone-soluble glue. Samples were removed from the carrier glass using acetone prior to microthermometry measurements. Due to the excellent cleavage of barite, care was taken so that only pristine fluid inclusions distal to internal fractures were selected. Measurements were made using Linkam® THMS 600 heating-freezing stages at GEOMAR and at the Department of Geosciences, University of Kiel. Each apparatus was mounted on a standard petrographic microscope with long working distance optics.

The heating-freezing stages were calibrated using SYNFLINC® synthetic fluid inclusion temperature standards. Accuracy and precision were estimated at ±0.2 °C near the triple point of CO_2 (±56.6 °C), and better than ±0.5 °C at other temperatures below ambient. Accuracy and precision for total homogenization measurements were estimated at ±2 °C.

Salinities were calculated using the following equation from Bodnar and Vityk (1994):

$$\text{Salinity(wt.\%)} = -1.78(T_m) + 0.0442(T_m)^2 - 0.000557(T_m)^3 \quad (1)$$

where T_m is the final melting temperature, in degrees Celsius, of the solid phase within the inclusion upon heating from below the freezing point. Formation, or trapping temperatures (T_t) were determined by applying a hydrostatic pressure correction to the homogenization temperatures (T_h), which is defined as the minimum temperature in which a single phase fluid is present in the inclusion. For pressure corrections, isochores were calculated using the FLUIDS software package (Bakker, 2003, 2012).

3.7. Geochemical modeling

Concentrations of free barium, strontium, calcium and sulfate, and saturation states of barite, anhydrite and amorphous silica, were determined as a function of temperature assuming mixing of 350 °C vent fluid and seawater (Table 1). Calculations were made using the modeling code EQ3/6 (Wolery, 1992; Wolery and Daveler, 1992) with mineral precipitation and equilibrium between H_2S–SO_4 and CO_2–CH_4 suppressed. Thermodynamic data used were from SUPCRT92 (Johnson et al., 1992), with data for $MgSO_4$ and $NaSO_4^-$ species added (McCollom and Shock, 1997).

4. RESULTS

4.1. Crystal morphology

Barite within hydrothermal vents at Endeavour occurs as a wide range of crystal habits, from well-formed tabular and bladed crystals to dendritic crystals (Fig. 3). The majority of samples contain barite that is not restricted to a single crystal morphology and crystals with different habits often occur in different areas of a single sample. However, samples can be grouped into four broad morphological categories defined by the dominant morphologies present: (1) well-formed, tabular crystals (Fig. 3A); (2) bladed crystals (Fig. 3B); (3) acicular and/or radiating tapered crystals (Fig. 3C); and (4) dendritic crystals (Fig. 3D). Barite crystals vary in size from <0.1 mm up to 2 mm, and the larger crystals tend to have a more euhedral (tabular or bladed) morphology. Sphalerite and pyrite are the most common sulfide minerals present in barite-rich samples. Sphalerite is the dominant sulfide phase in samples with tabular or bladed barite, whereas pyrite is more common in samples that contain smaller acicular or dendritic barite. Barite typically crystallizes into open pore spaces, precipitating on pre-existing sulfide minerals, with the exception of dendritic barite, which often occurs as outward-facing fans on the exterior of a sample (Fig. 3D). Amorphous silica is generally the only phase that precipitates after barite, although sulfide overgrowth or replacement of relict barite is also present.

Table 1
Fluid compositions used in mixing calculations.

	Endeavour vent fluid[a]	Seawater[b]
Temperature (°C)	350	2
pH (25 °C)	4.2	8
Mg mmol/kg	0	53.2
Cl mmol/kg	425	550
Na mmol/kg	320	460
Ca mmol/kg	32.7	10.3
K mmol/kg	24.4	10.2
SiO2 mmol/kg	15.7	0.1
Fe mmol/kg	915	0
Mn mmol/kg	289	0
Ba mmol/kg	31	0.1
Sr mmol/kg	134	87
SO_4 mmol/kg	0	28.3
H_2S mmol/kg	5.4	0
CO_2 mmol/kg	12.6	2.5
H_2 μmol/kg	42	Log $fO_2 = -0.759$
NH_3 μmol/kg	500	4
$^{87}Sr/^{86}Sr$	0.7034 [c]	0.7092 [d]

[a] Endeavour vent fluid chemistry is from the Grotto vent (Butterfield et al., 1994) with Ba from Seyfried et al. (2003), H_2 from Lilley et al. (1993), NH_3 of 500 as an approximate value.
[b] Seawater values from Butterfield et al. (1994), Seyfried et al. (2003) and Tivey (2004).
[c] This study (see text).
[d] From Butterfield et al. (2001).

4.2. Trace element content of barite

Whole rock Ba and Ca concentrations for 335 chimney samples are plotted in Fig. 4A (see Supplementary Table S1 for full results). The Ba and Ca concentrations reflect the amount of barite and anhydrite in each sample, respectively, and range from below detection limits up to

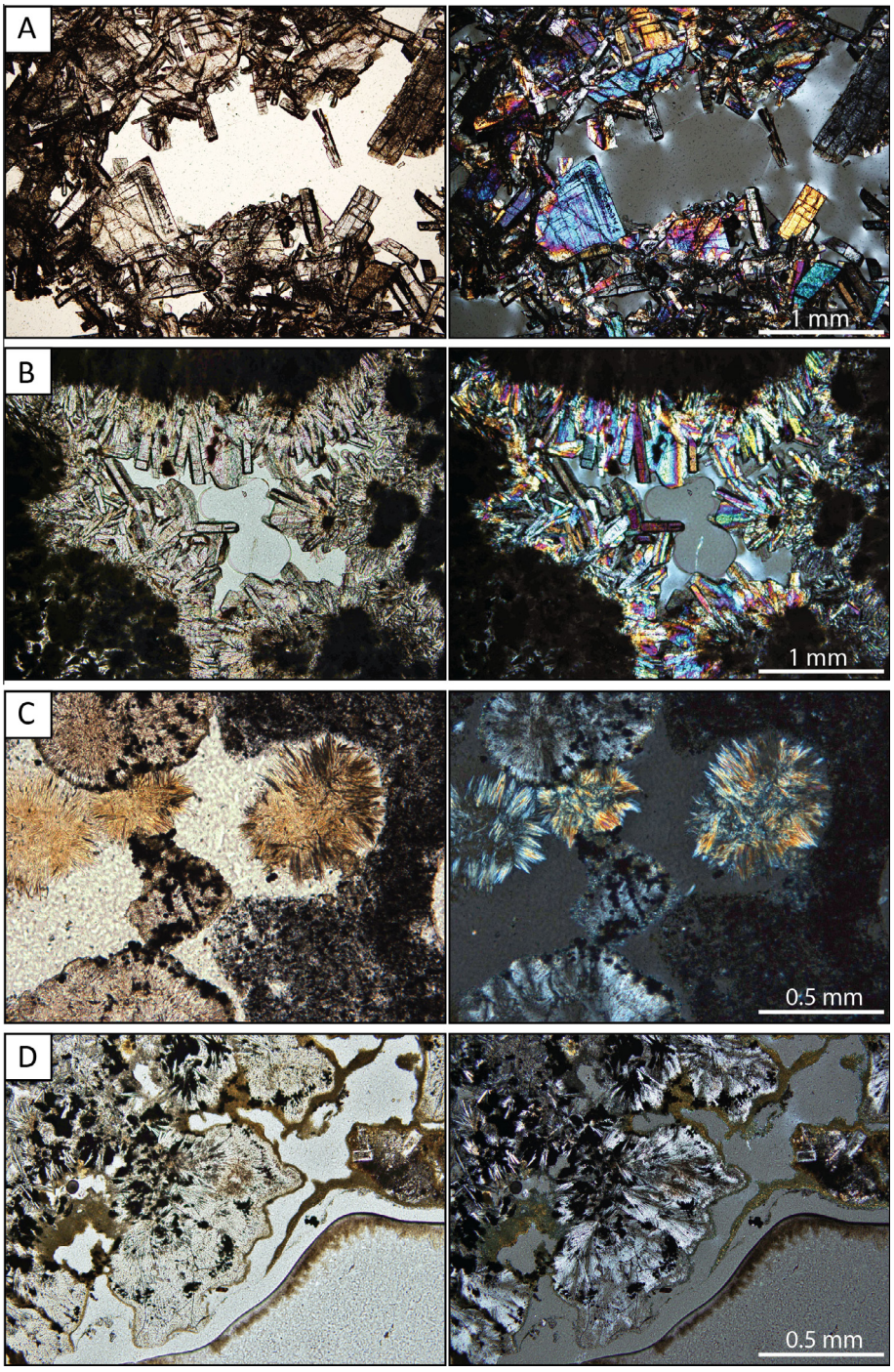

Fig. 3. Transmitted light photomicrographs (plane-polarized in left column, cross-polarized in right column) showing the range of crystal morphologies for barite crystals within hydrothermal vents from the Endeavour Segment. (A) Euhedral tabular and bladed crystals; (B) bladed crystals; (C) radiating acicular crystals; and (D) acicular and dendritic crystals.

~40 wt.% for both elements. The strong negative correlation between Ba and Ca is typical of hydrothermal vents in this and other locations (Koski et al., 1994; Hannington et al., 1995), and reflects the different saturation conditions under which barite and anhydrite precipitate within vents. The whole rock Sr concentrations are plotted against Ba in Fig. 4B. The samples are divided into those with either greater than or less than 1 wt.% Ca. For samples with less than 1 wt.% Ca, Sr concentrations range from 0 to 1.3 wt.% and there is a positive correlation between Sr and Ba ($R^2 = 0.74$). Samples that contain more than 1 wt.% Ca are generally Ba-poor, and contain up to only ~0.3 wt.% Sr, but show a similarly strong positive correlation between Ca and Sr ($R^2 = 0.83$). The strong correlations between Sr

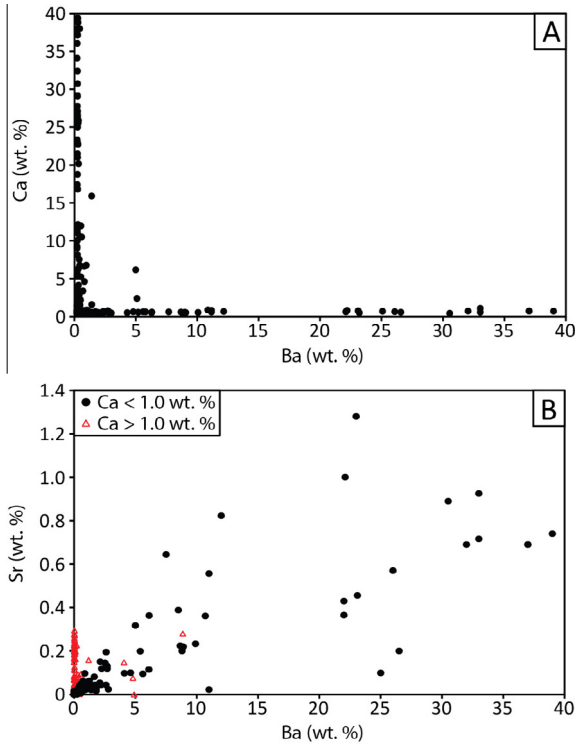

Fig. 4. (A) Plot of whole rock Ca vs. Ba for 335 chimney samples from all major vent fields and inactive vent sites within the axial valley showing a distinct negative correlation, with Ba-rich samples having low Ca concentrations, and Ca-rich samples having low Ba concentrations. Samples (B) Strontium concentration plotted against Ba concentration. Samples are grouped as either Ca-rich (red triangles) or Ca-poor (black circles). Because Sr partitions predominantly into anhydrite or barite, the low concentrations of Ca in the Ba-rich samples indicates that barite is the primary host for Sr in these samples, and whole rock Sr/Ba values are representative of the Sr/Ba content within the barite. (For interpretation of the references to colour in this figure legend, the reader is referred to the web version of this article.)

and both Ba and Ca indicate that barite and anhydrite are the primary mineral phases that host Sr in hydrothermal chimneys at Endeavour. Because Ba-rich samples are generally Ca-poor, the bulk of the Sr within Ba-rich samples will be contained within barite, and thus the reported whole rock $^{87}Sr/^{86}Sr$ ratios for Ba-rich samples are assumed to represent the Sr isotopic composition of barite within these samples.

Electron microprobe analysis of growth zones within individual barite crystals indicate that Sr and Ca are the major trace elements within barite and that the darker chemical zonations visible in the backscatter images reflect higher concentrations of Sr and Ca within the crystals (Fig. 5A and B). Strontium content (reported as percent relative to total Ba + Sr + Ca) ranges from 0% to 18%, with an average of 5.5% from 41 analyses. Calcium values are lower, and range from 0% to 10.9% and averages 1.9% ($n = 35$) (see Supplementary Table S2 and Fig. S1 for full results).

Trace element concentrations from laser ablation analysis of a single barite crystal from ALV2467-R2 are reported in Table 2 (lines A through H in Fig. 5C). Although concentrations of 61 elements were measured, only the elements with values above detection limits are included (see Supplementary Table S3 for results for all elements). The results are similar to the electron microprobe results, and indicate that concentrations of Sr, Ca and K are higher within the darker zones.

4.3. Hydrothermal fluid Sr concentrations and $^{87}Sr/^{86}Sr$ composition

The zero Mg endmember Sr isotope composition for vent fluids is determined by linear regression of $^{87}Sr/^{86}Sr$ ratio with Mg/Sr ratio and extrapolation to zero Mg/Sr (Butterfield et al., 2001). There is minor variation in the $^{87}Sr/^{86}Sr$ endmember between vent fields along the axis. When all samples are regressed together, the composite endmember for the whole segment is 0.70343 ± 0.00015. The majority of fluid samples were taken in the Main Endeavour Field (MEF), potentially biasing the results of the composite regression. When the endmember for each vent field is regressed independently, and then vent field endmembers averaged for the segment, a similar value of 0.70343 ± 0.00011 is obtained. This value is within the uncertainty range of the average $^{87}Sr/^{86}Sr$ value of 0.70329 ± 0.00037 (1-sigma) for hydrothermal fluids from mid-ocean ridge-hosted hydrothermal systems, based on measurements from the East Pacific Rise (Von Damm, 1990) and Mid-Atlantic Ridge (Von Damm, 1990; Elderfield et al., 1993; James et al., 1995; Gamo et al., 1996).

Endmember Sr concentrations generally vary with vent fluid chloride concentration (Seyfried et al., 2003). The average Sr concentrations of the endmembers for individual fields (using the same samples used for the Sr isotopic endmember) yields an average Sr concentration of 163 $\pm$ 52 μmol/kg.

4.4. Whole rock $^{87}Sr/^{86}Sr$ compositions

Whole rock Sr-isotope ($^{87}Sr/^{86}Sr$) ratios for 16 chimney samples are reported in Table 3. Ratios range from 0.703798 to 0.707581 and all fall between the values for Endeavour vent fluids (0.7034) and modern seawater (0.709183) (Butterfield et al., 2001). Higher $^{87}Sr/^{86}Sr$ ratios were generally found in samples dominated by dendritic and acicular barite crystals, whereas lower ratios were typical of samples containing dominantly well-formed, tabular crystals.

4.5. $^{87}Sr/^{86}Sr$ variations within barite crystals

Results of laser ablation analysis of discrete zones along single barite crystals in samples ALV2464-R4 and ALV2467-R2 are reported in Table 4 and plotted in Fig. 6 (locations of analyses are shown in Fig. 5D). For both crystals, there is a clear association between darker zones visible in the backscatter images and higher concentrations of Sr (open blue ovals), similar to the results from electron microprobe analyses.

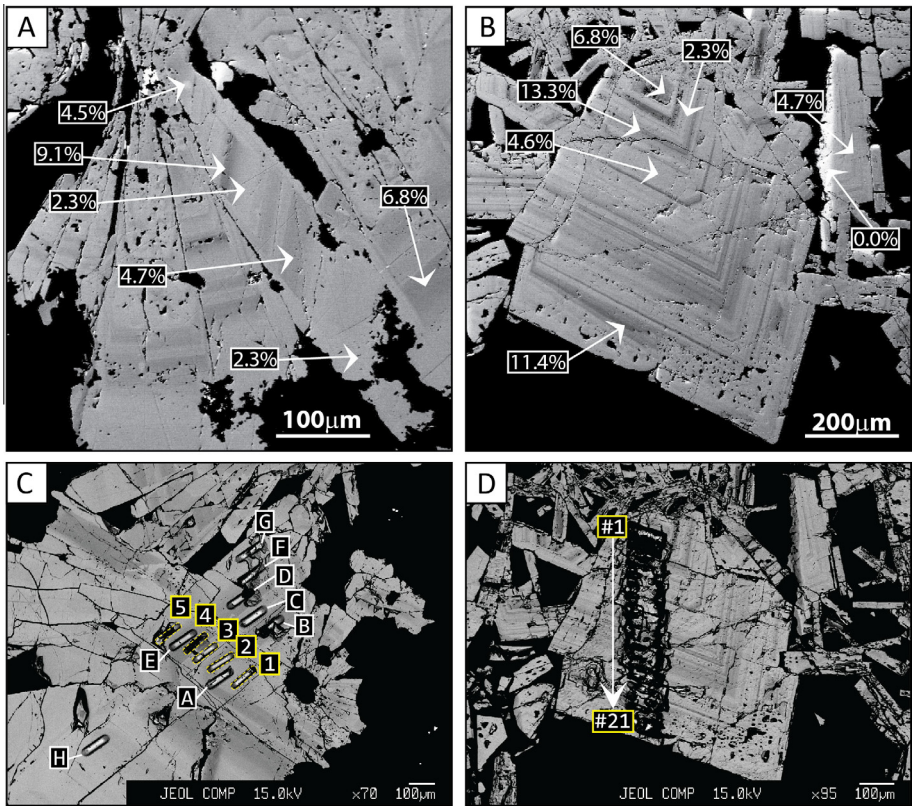

Fig. 5. Electron microprobe backscatter images of barite crystals from samples ALV2467-R2 (A and C) and ALV2464-R4 (B and D) showing Sr-rich (dark) and Sr-poor (light) growth zones. Numbers in A and B refer to the percent Sr occupying the cation site within barite, normalized to 100% Ba + Sr + Ca. Panels C and D show locations of laser ablation analyses. Lines A-H in C represent locations of elemental analyses summarized in Table 2. Lines 1–5 (C, outlined in yellow) and the closely-spaced parallel lines 1–21 (D) are locations of $^{87}Sr/^{86}Sr$ analyses, summarized in Table 4. (For interpretation of the references to colour in this figure legend, the reader is referred to the web version of this article.)

Table 2
Major element concentrations in barite from ALV2467-R2 (errors given in 2RSD %). Locations correspond to laser ablation tracks in Fig. 5C.

	Ba (ppm)	Sr (ppm)	Ca (ppm)	K (ppm)
Line A	583,466 ± 7%	17,140 ± 10%	4975 ± 13%	230 ± 15%
Line B	567,340 ± 7%	22,086 ± 7%	8933 ± 5%	352 ± 8%
Line C	561,626 ± 7%	13,380 ± 7%	4221 ± 7%	140 ± 10%
Line D	563,516 ± 8%	22,731 ± 8%	8176 ± 7%	286 ± 9%
Line E	588,013 ± 8%	25,708 ± 9%	11,367 ± 5%	419 ± 8%
Line F	558,996 ± 9%	14,176 ± 9%	4517 ± 8%	156 ± 13%
Line G	574,019 ± 8%	7403 ± 8%	1912 ± 8%	41 ± 22%
Line H	612,912 ± 7%	11,439 ± 11%	3528 ± 13%	101 ± 20%

For ALV2464-R4, $^{87}Sr/^{86}Sr$ values along the crystal are, with the exception of lines 16 and 21, within error of each other, and cluster around a value of 0.7046 (green dashed line) which represents the whole rock $^{87}Sr/^{86}Sr$ value for this sample (Table 3). Analyses #16 and #21 both sampled fluid inclusion-rich zones within the crystal (appear as dark pits in the backscatter image in Fig. 6). The $^{87}Sr/^{86}Sr$ values for these samples are higher than those for the rest of the crystal, suggesting that the inclusions may have trapped fluids that have a higher proportion of seawater than suggested by the surrounding crystal. There is a very weak negative correlation between Sr abundance in the crystal (recorded as Sr-intensity, which represents the relative concentration of Sr based on intensity of the output signal from the mass spectrometer) and $^{87}Sr/^{86}Sr$ values (Fig. 7). However, if analyses #16 and #21 are excluded, there is essentially no systematic variation in $^{87}Sr/^{86}Sr$ with Sr abundance in the crystal.

For ALV2467-R2, there is a smaller range in $^{87}Sr/^{86}Sr$ values than ALV2464-R4, and the values cluster near the whole-rock value of 0.7038 (Fig. 6). A negative correlation between $^{87}Sr/^{86}Sr$ values and Sr concentration is slightly

Table 3
Bulk $^{87}Sr/^{86}Sr$, calculated fluid mixing and fluid mixture temperatures for hydrothermal chimneys samples.

Sample	Barite crystal habit	Vent field	$^{87}Sr/^{86}Sr \pm 2\sigma$	% hydrothermal fluid[a]	Temperature of fluid mixture (°C)[b]	[Sr]/[Ba] (Whole Rock)[c]	[Sr]/[Ba] (Fluid)[d]	Apparent K_D[e]
ALV1452-1A	Dendritic	Main Endeavour	0.707581 ± 0.000011	17	61	0.069	2.62	0.004
ALV4446-1628	Acicular/bladed	Main Endeavour	0.706058 ± 0.000009	39	136	0.050	2.53	0.006
ALV3589-R2	Small tabular	Main Endeavour	0.705635 ± 0.000010	46	162	0.051	2.52	0.007
ALV4450-1829	Acicular/bladed	Mothra	0.705461 ± 0.000009	49	173	0.045	2.52	0.007
ALV2072-7	Acicular	Main Endeavour	0.705116 ± 0.000010	56	196	0.063	2.51	0.010
ALV2467-R3	Acicular/bladed	Clam Bed	0.704816 ± 0.000011	62	218	0.008	2.50	0.001
ALV2068-1	Acicular/bladed	Main Endeavour	0.704779 ± 0.000010	63	221	0.056	2.50	0.010
ALV2461-R6-4	Acicular	High Rise	0.704630 ± 0.000010	66	233	0.025	2.50	0.004
ALV2464-R4	Tabular	High Rise	0.704584 ± 0.000009	67	237		2.50	
ALV3000C	Acicular	Salty Dawg	0.704545 ± 0.000009	68	240	0.021	2.50	0.004
ALV2415-1D (3)	Acicular	Main Endeavour	0.704525 ± 0.000010	69	242	0.048	2.50	0.009
ALV1452-2	Acicular	Main Endeavour	0.704496 ± 0.000007	70	244	0.046	2.50	0.008
ALV2449-1	Acicular	Main Endeavour	0.704380 ± 0.000010	72	254	0.018	2.50	0.003
TiveyMisc2	Small tabular	Main Endeavour	0.704198 ± 0.000012	77	270	0.022	2.50	0.004
ALV2467-R9	Tabular	North of Clam Bed	0.703862 ± 0.000011	86	301	0.026	2.49	0.005
ALV2467-R2	Tabular	North of Main Endeavour	0.703798 ± 0.000009	88	308	0.020	2.49	0.004

[a] % relative contribution calculated using Eq. (2).
[b] Temperatures are calculated using Eq. (3).
[c] Ratio determined using whole rock Sr and Ba concentrations (see Supplementary Table S1).
[d] Calculated based on the degree of mixing (using $^{87}Sr/^{86}Sr$) between endmember seawater and hydrothermal fluids (see Table 1 for details).
[e] $D_{Sr} = ([Sr]/[Ba])_{Whole\ Rock}/([Sr]/[Ba])_{Fluid}$.

Table 4
Laser ablation strontium isotope ratios ($^{87}Sr/^{86}Sr$) across single barite crystals from samples ALV2464-R4 and ALV2467-R2.

Analysis[a]	$^{87}Sr/^{86}Sr \pm 2\sigma$	Relative Sr intensity[b] $\pm 2\sigma$	% hydrothermal fluid[c]	Temperature[d] (°C)
ALV2464-R4				
1	0.70447 ± 0.00022	4.73 ± 0.14	70	246
2	0.70468 ± 0.00026	3.36 ± 0.11	65	229
3	0.70434 ± 0.00029	4.27 ± 0.15	73	257
4	0.70456 ± 0.00029	4.60 ± 0.16	68	239
5	0.70442 ± 0.00026	4.74 ± 0.12	71	250
6	0.70453 ± 0.00024	3.67 ± 0.02	69	241
7	0.70447 ± 0.00027	5.55 ± 0.05	70	246
8	0.70438 ± 0.00024	3.23 ± 0.03	72	253
9	0.70449 ± 0.00020	2.60 ± 0.01	70	245
10	0.70413 ± 0.00020	4.71 ± 0.02	79	275
11	0.70439 ± 0.00026	5.07 ± 0.04	72	253
12	0.70431 ± 0.00027	5.42 ± 0.06	74	260
13	0.70445 ± 0.00027	6.75 ± 0.04	71	248
14	0.70442 ± 0.00025	5.81 ± 0.05	71	250
15	0.70428 ± 0.00025	4.06 ± 0.03	75	263
16	0.70485 ± 0.00022	3.09 ± 0.04	62	216
17	0.70421 ± 0.00023	4.44 ± 0.04	77	268
18	0.70436 ± 0.00025	7.83 ± 0.03	73	255
19	0.70436 ± 0.00021	8.14 ± 0.12	73	256
20	0.70463 ± 0.00025	2.62 ± 0.12	66	233
21	0.70509 ± 0.00025	1.34 ± 0.04	56	198
ALV2467-R2				
1	0.70394 ± 0.00021	4.22 ± 0.05	84	294
2	0.70373 ± 0.00018	5.80 ± 0.04	90	314
3	0.70401 ± 0.00019	4.04 ± 0.01	82	287
4	0.70392 ± 0.00022	6.04 ± 0.01	84	295
5	0.70435 ± 0.00025	1.91 ± 0.03	73	257

[a] Analysis numbers correspond to locations shown on Fig. 5D.
[b] Relative Sr intensity, measured during laser ablation analysis can be used as a proxy for Sr-concentration within the barite crystal.
[c] % hydrothermal fluid is calculated using Eq. (2).
[d] Temperature is calculated using Eq. (3).

more pronounced for this sample (Fig. 7), suggesting that the partitioning of Sr into the barite lattice is greater when the source fluid has a higher proportion of hydrothermally-derived Sr.

4.6. Microthermometry

Fluid inclusions were investigated in barite and in interstitial amorphous silica from samples ALV2464-R4 and ALV2467-R2. These samples contain both liquid-dominated and vapour-dominated 2-phase liquid (L) + vapour (V) inclusions at ambient temperatures (Fig. 8). In rare cases, metastable single-phase L inclusions that nucleated a vapour bubble upon cooling below room temperature were encountered. The overall size of individual fluid inclusions ranges from <1 μm to ~30 μm. However, microthermometry measurements were made only on inclusions between 2 and 10 μm in size.

Fluid inclusions within the barite crystals can be texturally classified as either primary or secondary. Primary inclusions occur either as solitary inclusions or small clusters that are well removed from grain boundaries, or as trails within growth zones of the host mineral that do not approach grain boundaries (Fig. 8A and B). Secondary fluid inclusions occur as trails in healed cracks crosscutting growth zones (if applicable) and ending at the surface boundary of the respective crystal (Fig. 8C). The terms "primary" and "secondary" inclusions as used here apply to single crystals (and in rare cases to their immediate surroundings), and thus do not necessarily imply that all primary inclusions in a given sample were formed earlier than secondary inclusions. Rare fluid inclusions also occur in interstitial spaces between amorphous silica globules (Fig. 8D).

Within each sample, most primary fluid inclusions and many of the secondary inclusions are liquid dominated (i.e. they have vapour bubble sizes comprising less than ~30% of the inclusion volume). A sub-set of secondary inclusions form trails that include vapour-dominated inclusions as well. Careful microscopic investigations indicate that neighbouring liquid-dominated fluid inclusions within many growth zones and secondary trails have variable L/V phase proportions, which is a strong indication of post-entrapment modification upon cooling, involving progressive crack healing, or necking down, after initial bubble formation of the host mineral (Roedder, 1984). Therefore, only inclusion trails where neighbouring inclusions have similar L/V phase proportions, and were therefore assumed to represent the original densities, were selected for microthermometry measurements.

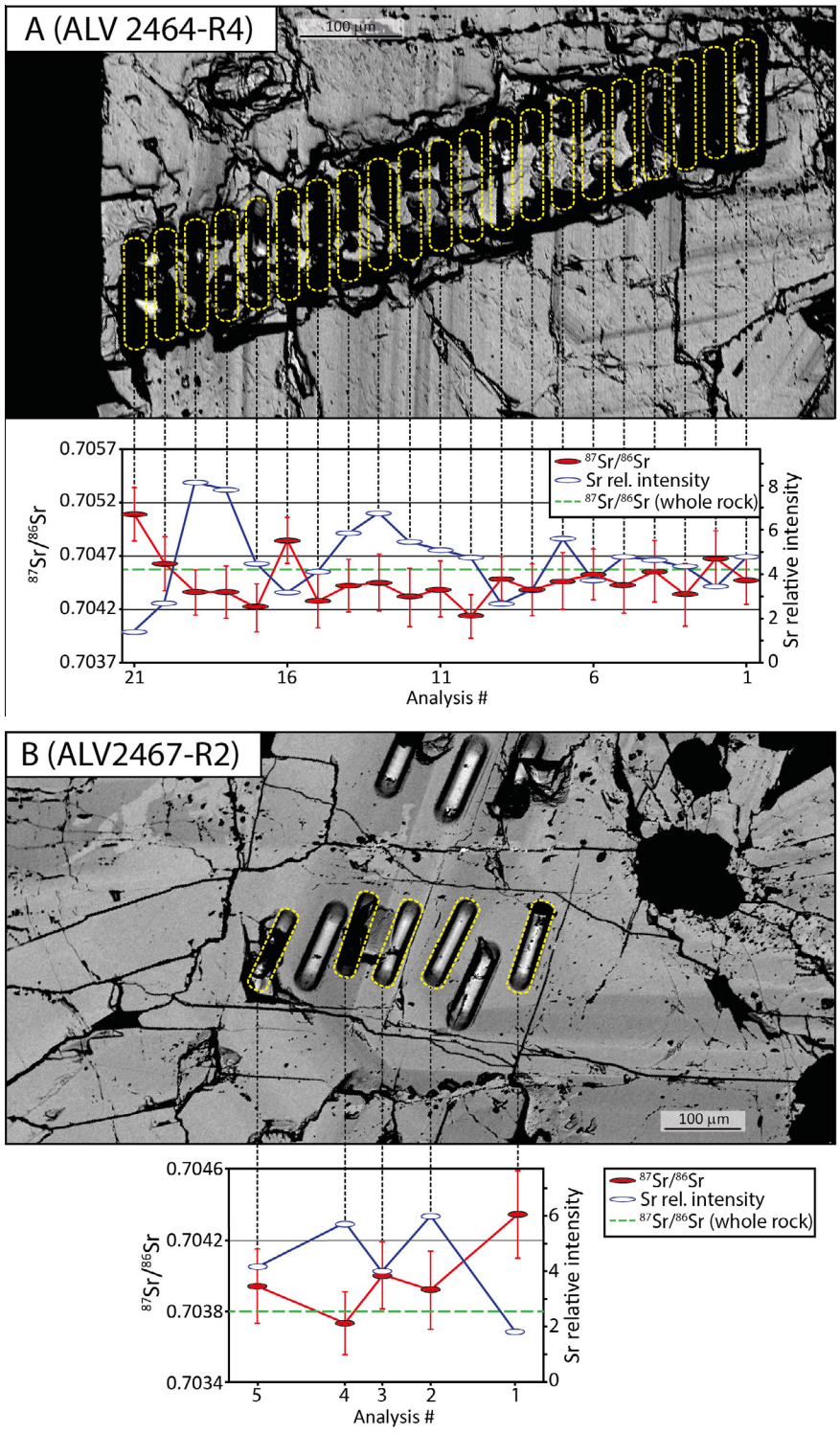

Fig. 6. Results of $^{87}Sr/^{86}Sr$ variability and Sr-concentrations within single barite crystals from ALV2464-R4 (A) and ALV2467-R2 (B). The locations of the laser raster for each analysis are outlined on the associated backscatter. For ALV2467-R2, the rasters not outlined in yellow are from elemental analyses indicated in Fig. 5C. The relationship between Sr concentration and zonation within the crystals can be clearly seen, with darker regions having a higher Sr/Ba. The width of each data point on the plots is equal to the width of each ablation line (25 µm). Uncertainties for relative Sr concentrations are smaller than the symbols. (For interpretation of the references to colour in this figure legend, the reader is referred to the web version of this article.)

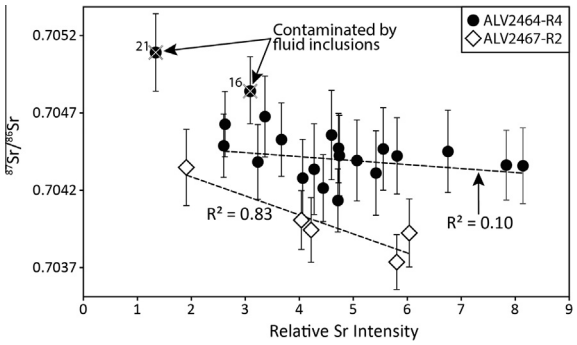

Fig. 7. Plot of $^{87}Sr/^{86}Sr$ versus the relative intensity of Sr (a proxy for Sr-concentration based on the relative strength of the Sr signal from the mass spectrometer) for samples ALV2464-R4 and ALV2467-R2. For ALV2464-R4 (black circles), there is very little variation in Sr-isotope composition with concentration within the crystal. Analyses 16 and 21 were ignored when plotting the regression line, as these samples were contaminated by large fluid inclusions. For ALV2467-R2 (open diamonds), a slight negative correlation is present, indicating a decreasing contribution of seawater (lower $^{87}Sr/^{86}Sr$) with higher Sr/Ba in the crystal.

Upon cooling, the liquid-dominated fluid inclusions froze to aggregates of ice and vapour at temperatures between −35 °C and −55 °C. Once frozen, the vapour bubbles within inclusions containing a vapour phase of less than about 10 vol.% were squeezed out of existence due to expansion of the aqueous phase during the water to ice transition. Further cooling to about −70 °C to −110 °C produced no further phase changes, implying that gaseous species such as CO_2 or CH_4 can only be present in amounts less than about 5 mol%, if at all (Konnerup-Madsen, 1995). Upon heating the inclusions, initial melting (T_i) occurred between −35 °C and −21 °C, which is close to the eutectic point in a NaCl–H_2O-dominated system. The lower T_i values suggest the presence of variable amounts of minor species other than NaCl in the system. Final melting temperatures (T_m) for inclusions in barite ranged between −5.4 °C and −3.5 °C. Using Eq. (1), final melting temperatures correspond to an average salinity of 7.6 ± 1.1 wt.% NaCl equivalent (1-sigma, $n = 8$) for ALV2464-R4 and 6.6 ± 1.2 wt.% NaCl equivalent (1-sigma, $n = 2$) for ALV2467-R2 (Bodnar and Vityk, 1994; Bakker, 2012) (Table 5). A final melting temperature of −2.0 °C from a single inclusion within amorphous silica from ALV2464-R4 corresponds to a NaCl equivalent salinity of 3.4 wt.%, which is near seawater values (Bodnar and Vityk, 1994; Bakker, 2012).

Final homogenization temperatures of liquid + vapour (L + V) into liquid occur at temperatures between 114 °C and 269 °C for the dominantly secondary inclusions within barite ($n = 64$), and 118–127 °C for inclusions within amorphous silica ($n = 5$) (see Supplementary Table S5 for full results). Sample water depths of about 2200 m corresponds to a pressure of 22 MPa (220 bar), and translates into pressure corrections of 10–14 °C and corrected formation temperatures of 124–283 °C and 128–137 °C for barite- and amorphous silica-hosted inclusions, respectively (Fig. 9). The highest formation temperatures in both samples correspond to primary inclusions within large, blocky (euhedral) crystals. Lower formation temperatures are associated with secondary liquid dominated inclusions, and primary inclusions in smaller, dendritic crystals.

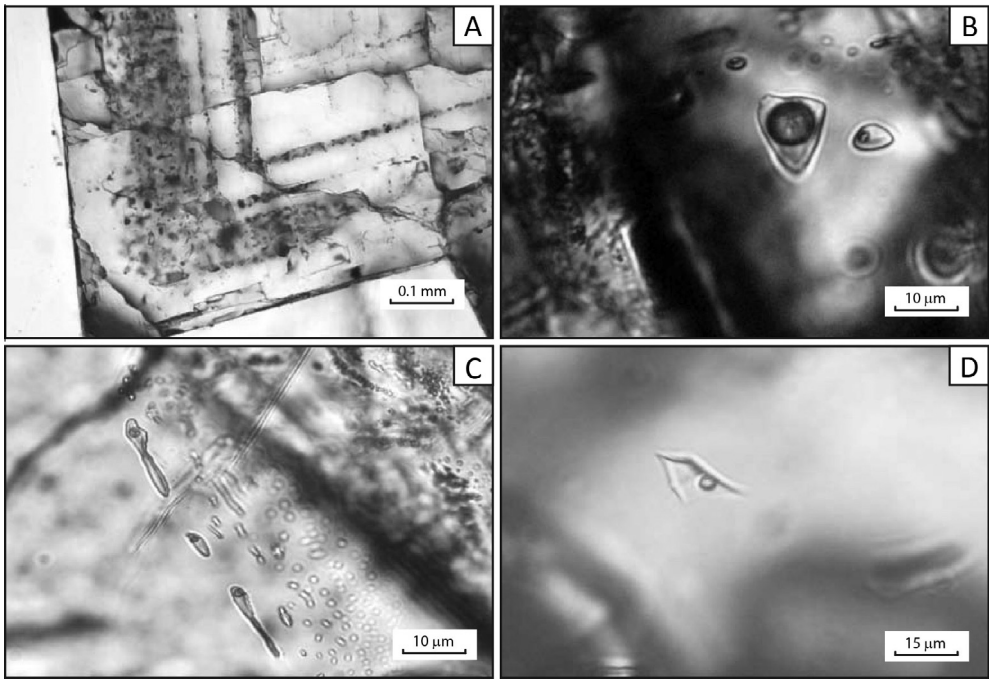

Fig. 8. Occurrence of aqueous fluid inclusions in barite and amorphous silica. (A) Tabular, zoned barite crystal comprising several growth zones delineated by primary fluid and solid inclusions. (B) Primary fluid inclusions in barite with variable vapor/liquid ratios. (C) Late secondary ("immature") inclusions in barite. (D) Inclusions in amorphous silica.

Table 5
Calculated fluid salinities from fluid inclusions.

Inclusion #	Final melting temperature (T_m, °C)	Salinity (wt.%)[1]
ALV2464-R4 (Barite)		
1	−5.1	8.0
2	−3.8	6.2
3	−5.1	8.0
4	−5.3	8.3
5	−5.4	8.4
6	−4.6	7.3
7	−5.6	8.7
8	−3.5	5.7
ALV2467-R2 (Barite)		
1	−3.5	5.7
2	−4.7	7.4
ALV2464-R4 (Amorph. Silica)		
1	−2.0	3.4

[1] Calculated using Eq. (1).

Due to the small sizes of vapour-dominated inclusions, no exact microthermometry measurements were possible. Melting reactions were visible between 1 °C and ~10 °C in two of the inclusions, which may correspond to melting of a gas hydrate, and thus indicate the presence of a gaseous component like CO_2 or CH_4 in the original vapour phase.

Secondary fluid inclusions are both liquid- and vapour-dominated, indicating that later-stage venting comprised two or more stages, with at least one stage comprising vapour-rich (i.e. low-density) fluids. Formation temperatures for secondary inclusions are typically lower than those for primary inclusions, and cluster between ~130 °C and 170 °C. Secondary inclusions are also found in smaller, less well-formed crystals, which is consistent with results of geochemical modelling that links less well-formed crystals to higher degrees of fluid supersaturation at lower temperatures (see discussion on crystal morphology below). Direct venting of a vapour phase has been reported at Endeavour; however these venting events have been short-lived and associated with episodes of venting of fluids with temperatures at or above the seawater boiling curve (Butterfield et al., 1994; Seyfried et al., 2003; Kelley et al., 2012).

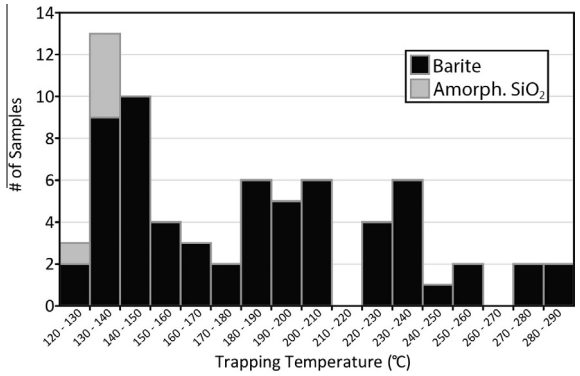

Fig. 9. Histogram of pressure-corrected fluid inclusion formation temperatures for barite and amorphous silica. The majority of primary inclusions from well-formed barite crystals indicate formation temperatures of between 180 °C and 240 °C. Secondary barite inclusions and inclusions within amorphous silica formed at lower temperatures (130–170 °C). Only the smallest, smooth-walled workable inclusions were used, and care was taken during the homogenization measurements, observing continuously during heating, to avoid possible overheating and stretching of the inclusions. However, the large range of homogenization temperatures may reflect an increase in volume upon heating.

Formation temperatures of 120–140 °C for amorphous silica are consistent with previous estimates by Tivey and Delaney (1986) and, along with measured fluid salinity near that of seawater, are consistent with precipitation towards the exterior of the chimney walls.

5. DISCUSSION

5.1. Fluid Mixing

The measured $^{87}Sr/^{86}Sr$ values within hydrothermal barite in this study (both whole rock and laser ablation spot analyses) lie between the endmember values for seawater and Endeavour hydrothermal fluid (Table 1), and record the amount of mixing between these two endmember fluids at the sites of barite precipitation within vent chimney walls. The relative contribution of each endmember fluid can be quantified by applying a two component mixing model:

$$\%HF = 100 \times \frac{[Sr]_{SW}\left[(^{87}Sr/^{86}Sr)_{SW} - (^{87}Sr/^{86}Sr)_{BA}\right]}{[Sr]_{SW}\left[(^{87}Sr/^{86}Sr)_{SW} - (^{87}Sr/^{86}Sr)_{BA}\right] + [Sr]_{HF}\left[(^{87}Sr/^{86}Sr)_{BA} - (^{87}Sr/^{86}Sr)_{HF}\right]} \quad (2)$$

Stretching of barite during heating commonly produces a measurable increase in volume and an increase in homogenization temperature (Ulrich and Bodnar, 1988). This likely accounts for some of the highest homogenization temperatures in Fig. 9. However, the results correspond closely to the inferred temperatures of barite formation from both thermal mixing and solubility calculations (see below).

where % HF is the proportion of hydrothermal fluid (with the remaining proportion being seawater), $[Sr]_{SW}$ and $[Sr]_{HF}$ are the Sr concentrations of seawater and the hydrothermal fluid, respectively, and $(^{87}Sr/^{86}Sr)_{SW}$, $(^{87}Sr/^{86}Sr)_{HF}$ and $(^{87}Sr/^{86}Sr)_{BA}$ are the Sr-isotope ratios for seawater, hydrothermal fluid and barite, respectively (Mills et al., 1998). This model assumes that there is no

fractionation of Sr isotopes during precipitation of barite. An investigation by Widanagamage et al. (2014) of Sr-isotope fractionation during synthetic barite precipitation at temperatures of up to 40 °C indicated a maximum fractionation (difference in $^{87}Sr/^{86}Sr$ between barite and solution) of ~0.0002, which is equivalent to or less than the analytical uncertainty of the measurements presented in this study (Tables 3 and 4). Fractionation factors for barite precipitation in hydrothermal chimneys would likely be much smaller than those reported by Widanagamage et al., due to higher temperatures.

The relative contributions of each endmember fluid that resulted in barite precipitation, based on Eq. (2), varies from 17% to 88% hydrothermal fluid, and averages 62% (Table 1). For comparison, Kusakabe et al. (1990) report hydrothermal contributions of between 80% and 90% for hydrothermal barite from the Mariana backarc basin using a similar approach. The relative contributions of each endmember fluid can be combined with the physical and chemical properties of the endmember fluids to infer the physical and chemical conditions under which barite precipitated within the chimney walls.

5.2. Conditions of barite formation

The fluid temperature within a chimney wall is dependent on the combined effects of the amount of mixing between hot hydrothermal fluid and cold seawater and conductive cooling of the hydrothermal fluid or heating of seawater. If considering only the temperature effects of fluid mixing, the temperature at which barite precipitates can be inferred using a linear thermal mixing relationship:

$$T = X(T_{HF} - T_{SW}) + T_{SW} \quad (3)$$

where T is the temperature of the mixed fluid in degrees Celsius, T_{HF} and T_{SW} are the temperatures of endmember hydrothermal fluid and seawater, respectively, also in degrees Celsius (Table 1), and X is the fraction of hydrothermal fluid in the mixture, calculated using Eq. (2) (Fig. 10) (Mills and Elderfield, 1995). The endmember hydrothermal fluid temperature of 350 °C represents average typical maximum vent fluid temperatures at Endeavour (Seyfried et al., 2003; Kelley et al., 2012). Temperatures of up to 375 °C have been recorded at MEF, and represent the thermodynamic maximum temperature of seawater defined by the hydrostatic pressure at that depth (220 bars at 2200 m), suggesting that these fluids are on the liquid–vapour phase boundary for seawater (Bischoff and Rosenbauer, 1985; Tivey et al., 1990; Delaney et al., 1992; Kelley et al., 2012). A short-lived episode of higher fluid temperatures (>400 °C) has been reported for the MEF, and is thought to represent a brief period of venting of a vapour phase (Tivey et al., 1990; Butterfield et al., 1994).

Calculated mixing temperatures using Eq. (3) range from 61 °C to 308 °C for 16 samples from the Endeavour Segment (Table 3). These values are comparable to previous estimates of the temperature range under which hydrothermal barite typically precipitates on the seafloor (e.g., ~100–300 °C) (Blount, 1977; Hannington et al., 1995).

The primary inclusions in the larger euhedral crystals of barite are liquid-dominated, indicating barite precipitation from a homogenous, high-density fluid. Trapping temperatures of the majority of the primary inclusions in the large crystals suggest likely barite formation at temperatures of

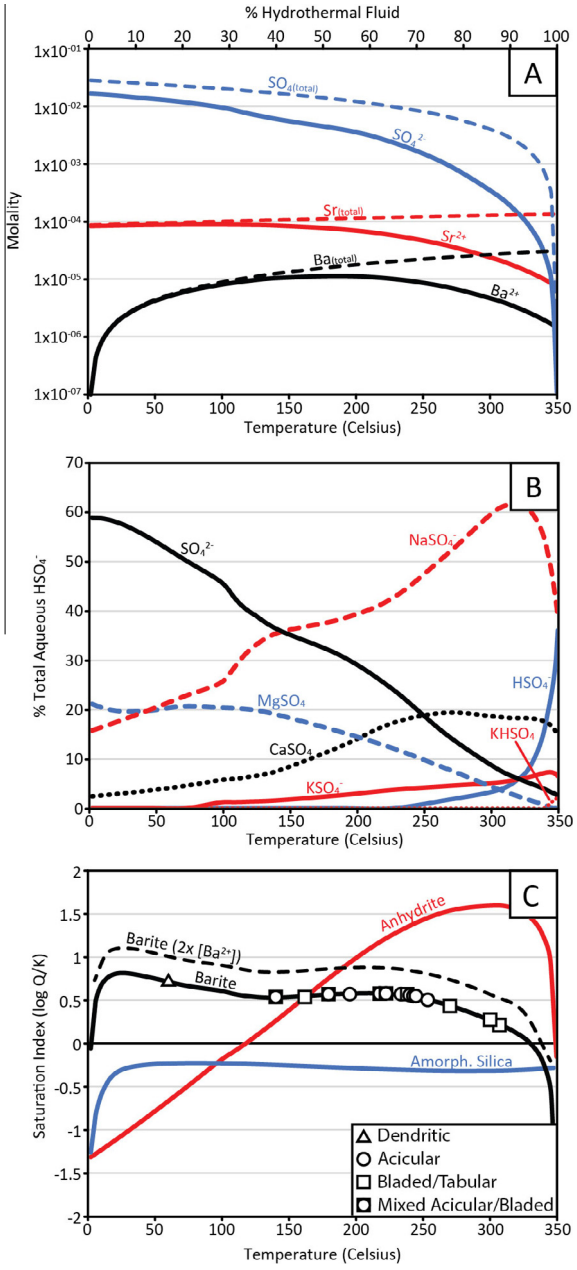

Fig. 10. Results of chemical modelling of fluid mixing. (A) Changes in free and total Ba^{2+}, Sr^{2+} and SO_4^{2-} concentrations as a function of both temperature and degree of mixing. (B) Variation in the relative proportions of different SO_4^{2-}-bearing species at different mixing temperatures. (C) Degree of super- or under-saturation of barite, anhydrite and amorphous silica as a function of fluid mixing temperature. Mineral precipitation occurs at saturation indices greater than zero. Samples are plotted based on mixing temperatures determined using barite $^{87}Sr/^{86}Sr$ values. Higher degrees of supersaturation result in formation of dendritic, as opposed to well-formed, barite.

between 180 °C and 240 °C (Fig. 9). These formation temperatures are consistent with previously reported temperatures for barite precipitation (e.g., Hannington and Scott, 1988; Halbach et al., 1989; Hannington et al., 1995), with the highest measured trapping temperatures possibly a result of stretching effects on the inclusions (Ulrich and Bodnar, 1988).

Measured fluid salinities from primary inclusions in barite from samples ALV2467-R2 and ALV2464-R4 are higher than that of seawater, suggesting that the vent fluid contained a component of a brine phase during barite formation for both samples (Coumou et al., 2009). Using the % hydrothermal fluids determined using bulk $^{87}Sr/^{86}Sr$ (summarized in Table 3), and a seawater salinity of 3.3 wt.%, the average salinity of 7.6 wt.% NaCl equivalent from sample ALV2464-R4 corresponds to a hydrothermal fluid with a salinity of 9.4 wt.%. For ALV2467-R2, the calculated hydrothermal fluid salinity is 7.1 wt.%. Phase separation is generally accepted to be an important control on fluid chemistry at MEF and High Rise; however, so far only venting of low-salinity fluids has provided any direct evidence of phase separation in the subsurface at these sites (Butterfield et al., 1994; Seyfried et al., 2003; Kelley et al., 2012). Venting of a high-salinity fluid has not been documented at MEF or High Rise, but the presence of a brine layer in the subsurface is predicted from mass-balance constraints (Butterfield et al., 1994; Seyfried et al., 2003) and from time-series temperature-salinity data (Larson et al., 2009). The high-salinity fluid inclusions presented here may be the first evidence of past venting of a high-salinity brine component at MEF and High Rise. The fluid inclusion temperature and salinity data from multiple chimneys suggest an overall early stage of higher-temperature barite precipitation from a homogenous, high-salinity fluid, followed by later-stage of lower temperature venting of an alternating low-density fluid (vapour phase) and a homogenous high-salinity fluid.

For samples ALV2464-R4 and ALV2467-R2, the calculated fluid inclusion trapping temperatures are lower than the predicted temperatures from fluid mixing by 56 °C and 119 °C, respectively. Conductive cooling within the chimney walls will result in fluid temperatures being lower than the value calculated based purely on fluid mixing (Hannington and Scott, 1988). If the calculated trapping temperatures from the fluid inclusion microthermometry are considered to represent the actual temperatures of barite precipitation, the temperature difference between the two methods represents the amount of conductive cooling of the hydrothermal fluid within the chimney walls. Hannington and Scott (1988) estimated a decrease in fluid temperature of 75 °C (from 350 °C to ~275 °C) from conductive cooling, followed by mixing with 50% seawater, allowing for the co-precipitation of barite and silica at 185 °C within the wall of a hydrothermal spire from Axial Seamount, which is also on the Juan de Fuca Ridge.

5.3. Geochemical modelling

The saturation state of the mixed fluid with respect to barite (and other minerals) at different stages of mixing and for different temperatures, fluid compositions and chemical speciation can be inferred from geochemical modelling of the mixing between Endeavour hydrothermal fluid and seawater (Fig. 10). Fig. 10A shows variation in the total concentrations of free- and total-dissolved Ba^{2+}, Sr^{2+}, and SO_4^{2-} as a function of both temperature and degree of mixing, using fluid properties summarized in Table 1. The concentrations of free species represent the amount of solute available for mineral precipitation. Ba^{2+} is the dominant barium species in the mixed fluid, especially at lower temperatures. At temperatures above ~200 °C, the relative abundance of $BaCl^+$ increases and the absolute concentration of Ba^{2+} begins to decrease, even though the total Ba in the fluid increases towards higher temperatures. Strontium follows a similar pattern, although, unlike Ba, higher concentrations of Sr are maintained at lower temperatures due to the relatively high abundance of dissolved Sr in seawater. The high concentration of SO_4^{2-} at low temperatures reflects the relatively high concentrations of sulfate in seawater and negligible sulfate in the hydrothermal fluid. However, the slightly irregular surface of the concentration profile in Fig. 10A is a result of the complex speciation of sulfate, involving several different cations (Fig. 10B). In particular, the sudden dip in free SO_4^{2-} concentration at ~100 °C is associated with greater amounts of $NaSO_4^-$.

The physicochemical conditions for precipitation or dissolution of barite can be quantified by determining the saturation index of the fluid (S.I. = log Q/K, where Q is the activity product and K is the equilibrium constant). An S.I. > 0 will result in mineral precipitation, and a S.I. < 0 will result in mineral dissolution. Saturation indices for barite, anhydrite and amorphous silica are plotted in Fig. 10C. According to the model, barite will precipitate from mixing fluid at temperatures of between ~5 °C and 330 °C. These temperatures correspond to fluid mixtures that contain as little as 1% hydrothermal fluid, and as much as 94% hydrothermal fluid, reflecting the very low solubility of barite. Anhydrite will precipitate from the fluid at mixing temperatures greater than ~120 °C. The model predicts that amorphous silica, which is often abundant within Endeavour hydrothermal vents (e.g., Fig. 2A) will never reach saturation and will not precipitate solely as a result of fluid mixing. The mixing model does not consider conductive cooling, which is required for precipitation of amorphous silica, but the effect on barite saturation can be inferred from Fig. 10. If parcels of mixed fluid cool conductively, the saturation index of barite would increase because free Ba^{2+} and free SO_4^{2-} in the mixed fluid would increase as the stabilities of $NaSO_4^-$ and $BaCl^+$ complexes decrease at lower temperatures.

The modeling results presented in Fig. 10 also do not consider the effects of mineral precipitation on fluid composition and saturation index. Because of the high degree of supersaturation of anhydrite relative to barite at high temperatures (Fig. 10C), anhydrite precipitation would remove sulfate from the solution within a chimney, inhibiting the precipitation of barite at these high temperatures, resulting in the typical association of anhydrite with high-temperature sulfide minerals (e.g., chalcopyrite, pyrrhotite) in the interior and barite with lower-temperature sulfide

minerals (pyrite, sphalerite) towards the exterior of a chimney (Hannington et al., 1995).

The Ba concentration of the hydrothermal fluid reported in Table 1 represents the maximum reported non-endmember value for the Main Endeavour Field. Because of its very low solubility, precipitation of barite reduces the amount of dissolved Ba during fluid sampling, and results in non-linear behavior when determining zero-Mg endmember values and, for this reason, endmember Ba concentrations are rarely reported (Seyfried et al., 2003). The concentration of Ba within Endeavour hydrothermal fluid is likely higher than the maximum reported value of 31 μmol/L (Seyfried et al., 2003). Reported endmember Ba concentrations at Lucky Strike, another E-MORB-hosted hydrothermal site, are comparable and range between 10 and 52 μmol/L (Charlou et al., 2000). However, in this case the authors also state that the reported concentrations likely represent minimum values. The highest reported endmember Ba concentration for a vent fluid is 119 μmol/L, from fluids sampled from the Edmond site, on the Central Indian Ridge (Kumagai et al., 2008). The high values at this site are also attributed to enriched Ba within the underlying source rocks. Whether or not this maximum reported concentration is representative of the actual endmember concentration is unclear. However, this value does point to the possibility of Ba concentrations at Endeavour (and other mid-ocean ridge hydrothermal sites) being significantly higher than the reported non-endmember values for Endeavour fluids. Even at endmember concentrations double the amount indicated in Table 1, barite precipitation is predicted to occur over roughly the same temperature range (Fig. 10C). The geochemical modelling confirms that Ba concentration is the limiting factor during barite precipitation in any fluid mixture that contains an excess of sulfate (the intersection of the Ba^{2+} and SO_4^{2-} curves in Fig. 10A).

5.4. Crystal morphology

Laboratory growth experiments have linked barite crystal morphology to crystal growth rates and the degree of supersaturation of Ba^{2+} and SO_4^{2-} in the crystallizing fluid (Shikazono, 1994; Judat and Kind, 2004; Li et al., 2007; Widanagamage et al., 2014). Dendritic crystals grow quickly as a result of diffusion-limited aggregation of solute atoms from highly supersaturated fluids (Turcotte, 1997). Well-formed crystals grow more slowly at lower degrees of supersaturation, predominantly from surface reaction precipitation mechanisms (Shikazono, 1994).

A comparison of dominant barite crystal morphology for samples from Endeavour with the degree of fluid mixing and S.I. (Fig. 10C; Table 3) shows a relationship consistent with the experimental results described above. A marked increase in S.I. occurs at temperatures between ~10 °C and 140 °C, which corresponds to greater free SO_4^{2-} concentration and coincides with a marked decrease in the stability of $NaSO_4^-$. The single sample that plots in this region (ALV1452-1A) contains mainly dendritic barite, which is generally in agreement with the experimental results of Shikazono (1994), although the magnitude of supersaturation is significantly less. This is likely a result of the highly dynamic fluid environment within a vent chimney wall as compared to static laboratory experiments. Shikazono (1994) demonstrated that, under static laboratory conditions of 150 °C and pressures equal to the vapour pressures of the aqueous solutions, barite that precipitates from a solution with an S.I. below 20 will result in well-formed barite crystals. Dendritic crystals will form from a solution with an S.I. larger than 20 (i.e. a higher degree of supersaturation). The results from this study suggest that, in the dynamic environment within vent chimney walls, dendritic barite forms at low temperatures and high inputs of seawater, resulting in a S.I. of above ~0.6. This relationship is consistent with the typical occurrence of dendritic barite along the outer margins of a vent (e.g., Fig. 3D).

5.5. Strontium partitioning

The degree of Sr substitution in barite, expressed as an apparent partition coefficient ($K_D = (Sr/Ba)_{barite}/(Sr/Ba)_{fluid}$), was calculated for individual samples using whole rock geochemical data and modelled fluid compositions (Table 3). Calculated K_D values are reported as "apparent" values because the rapid temperature changes and high fluid flow velocities associated with hydrothermal venting, as well as the occurrence of dendritic crystal morphologies associated with high degrees of supersaturation, indicate non-equilibrium conditions during barite crystallization (Shikazono, 1994). Trace element substitution within crystals is controlled by the composition of the crystallizing fluid, pressure, temperature and crystal growth rate (Sasaki and Minato, 1983; Hannington and Scott, 1988; Averyt and Paytan, 2003). However, the effects of these external factors on element partitioning within barite under hydrothermal conditions are not well constrained (Shikazono et al., 2012). Laboratory experiments and thermodynamic constraints for typical marine conditions (i.e. low-temperature) indicate that Sr substitution in barite increases with temperature (Hanor, 2000; Averyt and Paytan, 2003). Alternatively, under hydrothermal conditions, Shikazono et al. (2012) link increased Sr partitioning to higher degrees of supersaturation and fast crystal growth. Sasaki and Minato (1983) suggest that, from precipitation experiments at temperatures between ~25 °C and 60 °C, the degree of supersaturation has a stronger control on Sr partitioning than temperature. A comparison of Sr/Ba ratios to apparent partition coefficient shows no relationship between degree of mixing and Sr substitution, indicating that different degrees of mixing, and hence fluid composition, are not a primary control on Sr substitution (Fig. 11B).

Apparent partition coefficients for individual Sr-rich and Sr-poor zones within a single crystal were also determined using crystal chemistry derived from laser ablation (Table 2) and modeled fluid compositions (Table 6; Fig. 11B). The consistent $^{87}Sr/^{86}Sr$ across individual Sr-rich and Sr-poor growth zones (Fig. 6) provide further evidence that Sr partitioning in the barite is not controlled by fluid mixing. The pattern of Ca substitution mimics that of Sr, which suggests that the zonation is also not solely a result of temporal

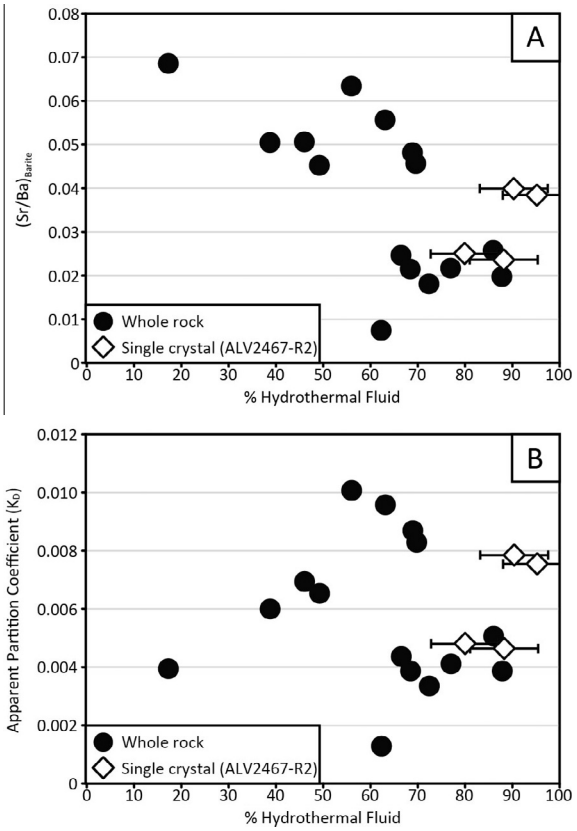

Fig. 11. Whole rock and single crystal Sr/Ba (A) and apparent partition coefficients (B) plotted against mixing temperature, showing a general decrease in Sr substitution at higher formation temperatures. Open diamonds represent Sr/Ba from different zones within a single euhedral barite crystal (Fig. 6B) and indicate variable Sr substitution over small changes in temperature. Whole rock temperature uncertainties are smaller than the symbol size, plotted temperature uncertainties for ALV2467-R2 are 2σ.

Table 6
Partition coefficients for individual growth zones within a single barite crystal from ALV 2467-R2.

Analyzed pair[a]	Sr/Ba (fluid)[b]	Sr/Ba (barite)[c]	Apparent K_D[d]
2 – B	5.09	0.04	0.008
3 – C	5.09	0.02	0.005
4 – D	5.09	0.04	0.008
5 – F	5.21	0.03	0.005

[a] Number/letter combinations refer to paired analyses from single growth zones in Fig. 5C.
[b] Calculated using predicted fluid chemistry based on degree of mixing (determined by $^{87}Sr/^{86}Sr$) and endmember fluid properties (Table 1).
[c] Calculated using data in Table 2.
[d] $K_D = ([Sr]/[Ba])_{Barite}/([Sr]/[Ba])_{Fluid}$.

variations in fluid Sr concentrations. Butterfield et al. (1994) report remarkably stable vent fluid chemistry at MEF over a 4-year period, although Lilley et al. (2003) and Seewald et al. (2003) report rapid changes in salinity in MEF following earthquakes and inferred magmatic activity. The higher abundance of fluid inclusions within the darker growth zones suggests that higher degrees of Sr substitution reflect periods of faster crystal growth, driven by increased conductive cooling and a higher degree of supersaturation. Changes in the amount of conductive cooling could result from oscillations in hydrothermal fluid flux. Without information on crystal growth rates, it is difficult to evaluate how much time is represented by each growth zone. However, the sharp boundaries between zones and oscillatory nature of the zonations suggest that the environmental factor(s) responsible for the zonations occur quickly and cyclically. The lighter zones are generally larger than the darker zones. This, coupled with the fact that crystal growth is likely faster during formation of the darker zones, indicates that conditions that favour lower levels of Sr substitution (i.e. the lighter zones; Fig. 5B) during crystal growth occur over longer periods of time than conditions that favour higher levels of Sr substitution.

6. CONCLUSIONS

The results of this study illustrate the utility of barite for recording physical and chemical processes associated with the formation of seafloor hydrothermal sulfide deposits. Specifically, barite records the temperature and chemical conditions that occur within vent chimney walls as a result of fluid mixing and conductive cooling. The occurrence of different crystal habits of barite within different parts of a chimney can provide a first order visual or petrographic tool for assessing the geochemical environment within chimney walls during active venting. A two-component mixing model based on $^{87}Sr/^{86}Sr$ compositions of barite from hydrothermal vents on the Endeavour Segment provides an effective means for quantifying the amount of fluid mixing that occurs within chimney walls. Results of Sr-isotope analyses indicate that, due to the very low solubility of barite, precipitation can occur over a wide range of mixing of hydrothermal fluid and seawater, with as little as a 17% hydrothermal fluid to as much as 88% hydrothermal fluid, and barite can precipitate at any stage during the growth history of a hydrothermal vent.

Precipitation of barite is controlled largely by the availability of free Ba^{2+} in the fluid mixture. High degrees of supersaturation associated with higher proportions of seawater result in crystal growth that is dominated by acicular and dendritic morphologies. Large, tabular and bladed crystals occur in more Ba-limited conditions in the interior regions of chimneys. Large euhedral crystals form at temperatures between ~120 °C and 240 °C, which are consistent with previous estimates for hydrothermal barite. A comparison of formation temperatures with modeled temperatures based on fluid mixing indicate that conductive cooling lowers the temperatures within the chimney walls by 60–120 °C, which will enhance barite precipitation.

Barite crystals also provide an effective record of fluid composition within chimney walls. Strontium zonation within single barite crystals that were originally thought to represent changes in fluid chemistry during crystal growth are instead attributed to temperature fluctuations,

and indicate that fluid chemistry is relatively stable over the growth periods of single crystals. Fluid salinity measurements from fluid inclusions trapped within barite crystals provide the first direct evidence of past venting of a fluid with a brine component from the Main Endeavour Field.

Unlike anhydrite, which has also been the focus of fluid mixing studies, barite is preserved on the seafloor and provides a record of fluid interaction in deposits from extinct hydrothermal systems on the seafloor and even ancient hydrothermal deposits on obducted oceanic crust. The physicochemical information recorded within barite that is outlined in this study can be used to evaluate the microbial habitat conditions and hydrothermal fluid properties in extinct deposits (e.g., Rasmussen, 2000; Golding et al., 2011). Comparative studies with barite hosted within ancient deposits may provide insights into ancient ocean chemistry and the formation of volcanogenic massive sulfide deposits (e.g., Jamieson et al., 2013b; Vearncombe et al., 1995).

ACKNOWLEDGEMENTS

The authors would like to thank Mario Thoner (GEOMAR) and Peter Jones (Carleton University) for their help collecting electron microprobe data, Elizabeth Ann Spencer (Carleton University) for help collecting Sr-isotope data, and Sven Petersen for many thoughtful discussions on hydrothermal chimney formation. Cora C. Wohlgemuth-Ueberwasser (Stockholm University) is gratefully acknowledged for providing the sulfide standard for laser ablation analysis. This work was supported by an NSERC PGS scholarship to JWJ and NSERC Discovery Grant to MDH. MKT acknowledges funding from NSF OCE-1130019. DAB acknowledges funding from NSF OCE-0731947 and the Joint Institute for the Study of the Atmosphere and Ocean (JISAO) under NOAA Cooperative Agreement NA10OAR4320148, contribution No. 2472, PMEL contribution No. 4399.

APPENDIX A. SUPPLEMENTARY DATA

Supplementary data associated with this article can be found, in the online version, at http://dx.doi.org/10.1016/j.gca.2015.10.021.

REFERENCES

Albarede F., Michard A., Minster J. F. and Michard G. (1981) Sr-87-Sr-86 ratios in hydrothermal waters and deposits from the East Pacific Rise at 21° North. *Earth Planet. Sci. Lett.* **55**, 229–236.

Averyt K. B. and Paytan A. (2003) Empirical partition coefficients for Sr and Ca in marine barite: implications for reconstructing seawater Sr and Ca concentrations. *Geochem. Geophys. Geosyst.* **4**, 1–14.

Baker E., German C. and Elderfield H. (1995) Hydrothermal plumes over spreading center axes: global distribution and geological inferences. *Geophys. Monogr.* **91**, 47–71.

Bakker R. J. (2003) Package FLUIDS 1. Computer programs for analysis of fluid inclusion data and for modelling bulk fluid properties. *Chem. Geol.* **194**, 3–23.

Bakker R. J. (2012) Package FLUIDS. Part 4: thermodynamic modelling and purely empirical equations for H_2O–NaCl–KCl solutions. *Mineral. Petrol.* **105**, 1–29.

Bischoff J. L. and Rosenbauer R. J. (1985) An empirical-equation of state for hydrothermal seawater (3.2% NaCl). *Am. J. Sci.* **285**, 725–763.

Blount C. W. (1977) Barite solubilities and thermodynamic quantities up to 300 °C and 1400 bars. *Am. Mineral.* **62**, 942–957.

Bodnar R. and Vityk M. (1994) Interpretation of microthermometric data for H_2O–NaCl fluid inclusions. In *Fluid Inclusions in Minerals, Methods and Applications* (eds. B. De Vivo and M. Frezzotti). Virginia Tech, Blacksburg, VA, pp. 117–130.

Butterfield D. A., Lilley M. D., Huber J. A., Roe K. K., Embley R. E., Baross J. A. and Massoth G. J. (2004) Mixing, reaction and microbial activity in the sub-seafloor revealed by temporal and spatial variation in diffuse flow vents at axial volcano. In *The Sub-seafloor Biosphere at Mid-ocean Ridges* (eds. W. S. D. Wilcock, D. S. Kelley, J. A. Baross, E. DeLong and C. Cary). American Geophysical Union.

Butterfield D. A., McDuff R. E., Mottl M. J., Lilley M. D., Lupton J. E. and Massoth G. J. (1994) Gradients in the composition of hydrothermal fluids from the Endeavour Segment vent field – Phase-separation and brine loss. *J. Geophys. Res. Solid Earth* **99**, 9561–9583.

Butterfield D. A., Nelson B. K., Wheat C. G., Mottl M. J. and Roe K. K. (2001) Evidence for basaltic Sr in midocean ridge-flank hydrothermal systems and implications for the global oceanic Sr isotope balance. *Geochim. Cosmochim. Acta* **65**, 4141–4153.

Chan L. H., Edmond J. M., Stallard R. F., Broecker W. S., Chung Y. C., Weiss R. F. and Ku T. L. (1976) Radium and barium at GEOSECS stations in Atlantic and Pacific. *Earth Planet. Sci. Lett.* **32**, 258–267.

Charlou J. L., Donval J. P., Douville E., Jean-Baptiste P., Radford-Knoery J., Fouquet Y., Dapoigny A. and Stievenard M. (2000) Compared geochemical signatures and the evolution of Menez Gwen (37 °50′N) and Lucky Strike (37 °17′N) hydrothermal fluids, south of the Azores Triple Junction on the Mid-Atlantic Ridge. *Chem. Geol.* **171**, 49–75.

Clague D. A., Caress D. W., Thomas H., Thompson D., Calarco M., Holden J. and Butterfield D. (2008) Abundance and distribution of hydrothermal chimneys and mounds on the Endeavour Ridge determined by 1-m resolution AUV multibeam mapping surveys. *Eos, Transactions, American Geophysical Union 89*. Fall Meet. Suppl., Abstract V41B-2079.

Coumou D., Driesner T., Weis P. and Heinrich C. A. (2009) Phase separation, brine formation, and salinity variation at Black Smoker hydrothermal systems. *J. Geophys. Res. Solid Earth* **114**, 1–16.

Cousens B. (2010) Igneous Rock Associations 11. The geology and petrology of seafloor volcanic rocks of the Northeastern Pacific Ocean, Offshore Canada. *Geosci. Canada* **37**, 49–64.

de Ronde C. E. J., Hannington M. D., Stoffers P., Wright I. C., Ditchburn R. G., Reyes A. G., Baker E. T., Massoth G. J., Lupton J. E., Walker S. L., Greene R. R., Soong C. W. R., Ishibashi J., Lebon G. T., Bray C. J. and Resing J. A. (2005) Evolution of a submarine magmatic-hydrothermal system: brothers volcano, southern Kermadec arc, New Zealand. *Econ. Geol.* **100**, 1097–1133.

Delaney J. R., Robigou V., McDuff R. E. and Tivey M. K. (1992) Geology of a vigorous hydrothermal system on the Endeavour Segment, Juan de Fuca Ridge. *J. Geophys. Res. Solid Earth* **97**, 19663–19682.

Ditchburn R., Graham I., Barry B. and de Ronde C. (2004) Uranium series disequilibrium dating of black smoker chimneys. *N. Z. Sci. Rev.* **61**, 54–56.

Ditchburn R. G., de Ronde C. E. J. and Barry B. J. (2012) Radiometric dating of volcanogenic massive sulfides and associated iron oxide crusts with an emphasis on Ra-226/Ba

and Ra-228/Ra-226 in volcanic and hydrothermal processes at intraoceanic arcs. *Econ. Geol.* **107**, 1635–1648.

Elderfield H., Mills R. A. and Rudnicki M. D. (1993) Geochemical and thermal fluxes, high-temperature venting and diffuse flow from mid-ocean ridge systems: the TAG hydrothermal field, Mid-Atlantic Ridge 26°N. *Geol. Soc. London Spec. Publ.* **76**, 295–307.

Fietzke J. and Frische M. (2016) Experimental evaluation of elemental behavior during LA-ICP-MS: influences of plasma conditions and limits of plasma robustness. *J. Anal. At. Spectrom.* http://dx.doi.org/10.1039/c5ja00253b.

Fietzke J., Liebetrau V., Guenther D., Guers K., Hametner K., Zumholz K., Hansteen T. H. and Eisenhauer A. (2008) An alternative data acquisition and evaluation strategy for improved isotope ratio precision using LA-MC-ICP-MS applied to stable and radiogenic strontium isotopes in carbonates. *J. Anal. At. Spectrom* **23**, 955–961.

Gamo T., Chiba H., Masuda H., Edmonds H. N., Fujioka K., Kodama Y., Nanba H. and Sano Y. (1996) Chemical characteristics of hydrothermal fluids from the TAG mound of the Mid-Atlantic Ridge in August 1994: implications for spatial and temporal variability of hydrothermal activity. *Geophys. Res. Lett.* **23**, 3483–3486.

Glickson, D.A., Kelley, D.S., Delaney, J.R., 2006. The Sasquatch Hydrothermal Field: Linkages Between Seismic Activity, Hydrothermal Flow, and Geology. American Geophysical Union, Fall Meeting 2006 Abstract #V23B-0614.

Glickson D. A., Kelley D. S. and Delaney J. R. (2007) Geology and hydrothermal evolution of the Mothra Hydrothermal Field, Endeavour Segment, Juan de Fuca Ridge. *Geochem. Geophys. Geosyst.* **8**, 1–23.

Golding S. D., Duck L. J., Young E., Baublys K. A., Glikson M. and Kamber B. S. (2011) Earliest seafloor hydrothermal systems on earth: comparison with modern analogues. In *Earliest Life on Earth: Habitats, Environments and Methods of Detection* (eds. S. D. Golding and M. Glikson). Springer, Netherlands, Amsterdam, Netherlands, pp. 15–49.

Goldstein S. J., Murrell M. T., Janecky D. R., Delaney J. R. and Clague D. A. (1991) Geochronology and petrogenesis of MORB from the Juan de Fuca and Gorda Ridges by U-238 Th-230 disequilibrium. *Earth Planet. Sci. Lett.* **107**, 25–41.

Halbach P., Nakamura K., Wahsner M., Lange J., Sakai H., Kaselitz L., Hansen R. D., Yamano M., Post J., Prause B., Seifert R., Michaelis W., Teichmann F., Kinoshita M., Marten A., Ishibashi J., Czerwinski S. and Blum N. (1989) Probably modern analog of Kuroko-type massive sulfide deposits in the Okinawa Trough back-arc basin. *Nature* **338**, 496–499.

Halevy I., Peters S. E. and Fischer W. W. (2012) Sulfate burial constraints on the phanerozoic sulfur cycle. *Science* **337**, 331–334.

Hannington, M., De Ronde, C., Petersen, S., 2005. Sea-Floor Tectonics and Submarine Hydrothermal Systems. Economic Geology 100th Anniversary Volume, pp. 111–141.

Hannington M., Herzig P., Scott S., Thompson G. and Rona P. (1991) Comparative mineralogy and geochemistry of gold-bearing sulfide deposits on the midocean ridges. *Mar. Geol.* **101**, 217–248.

Hannington M., Jonasson I., Herzig P. and Petersen S. (1995) Physical and chemical processes of seafloor mineralization at mid-ocean ridges. *Geophys. Monogr.* **11**, 115–157.

Hannington M. D. and Scott S. D. (1988) Mineralogy and geochemistry of a hydrothermal silica sulfide sulfate spire in the caldera of Axial Seamount, Juan-de-Fuca Ridge. *Can. Mineral.* **26**, 603–625.

Hanor J. S. (2000) Barite-celestine geochemistry and environments of formation. In *Reviews in Mineralogy & Geochemistry – Sulfate Minerals*, Vol. 40 (eds. C. N. Alpers, J. L. Jambor and D. K. Nordstrom). Mineralogical Society of America, Washington, D.C., pp. 193–275.

Humphris S. E. and Bach W. (2005) On the Sr isotope and REE compositions of anhydrites from the TAG seafloor hydrothermal system. *Geochim. Cosmochim. Acta* **69**, 1511–1525.

James R. H., Elderfield H. and Palmer M. R. (1995) The chemistry of hydrothermal fluids from the Broken Spur site, 29 °N Mid-Atlantic Ridge. *Geochim. Cosmochim. Acta* **59**, 651–659.

Jamieson J. W., Clague D. A. and Hannington M. D. (2014) Hydrothermal sulfide accumulation along the Endeavour Segment, Juan de Fuca Ridge. *Earth Planet. Sci. Lett.* **395**, 136–148.

Jamieson J. W., Hannington M. D., Clague D. A., Kelley D. S., Delaney J. R., Holden J. F., Tivey M. K. and Kimpe L. E. (2013a) Sulfide geochronology along the Endeavour Segment of the Juan de Fuca Ridge. *Geochem. Geophys. Geosyst.* **14**, 2084–2099.

Jamieson J. W., Wing B. A., Farquhar J. and Hannington M. D. (2013b) Neoarchaean seawater sulphate concentrations from sulphur isotopes in massive sulphide ore. *Nat. Geosci.* **6**, 61–64.

Johnson J. W., Oelkers E. H. and Helgeson H. C. (1992) SUPCRT92 - A software package for calculating the standard molal thermodynamic properties of minerals, gases, aqueous species, and reactions from 1-bar to 5000-bar and 0 °C to 1000 °C. *Comput. Geosci.* **18**, 899–947.

Judat B. and Kind M. (2004) Morphology and internal structure of barium sulfate - derivation of a new growth mechanism. *J. Colloid Interface Sci.* **269**, 341–353.

Karsten J. L., Delaney J. R., Rhodes J. M. and Liias R. A. (1990) Spatial and temporal evolution of magmatic systems beneath the Endeavour Segment, Juan de Fuca Ridge – Tectonic and petrologic constraints. *J. Geophys. Res. Solid Earth Planets* **95**, 19235–19256.

Kelley D. (2015) *Processed Bathymetry Grids (NetCDF:GMT Format) Derived from Ship-Based Multibeam Sonar Data from the Juan de Fuca Spreading Center Endeavour Segment Acquired during the Thomas G. Thompson Expedition TN146 (2002)*. Integrated Earth Data Applications (IEDA). http://doi.org/10.1594/IEDA/314300.

Kelley D. S., Carbotte S. M., Caress D. W., Clague D. A., Delaney J. R., Gill J. B., Hadaway H., Holden J. F., Hooft E. E. E., Kellogg J. P., Lilley M. D., Stoermer M., Toomey D., Weekly R. and Wilcock W. S. D. (2012) Endeavour Segment of the Juan de Fuca Ridge One of the most remarkable places on Earth. *Oceanography* **25**, 44–61.

Kelley D. S., Delaney J. R. and Yoerger D. R. (2001) Geology and venting characteristics of the Mothra hydrothermal field, Endeavour segment, Juan de Fuca Ridge. *Geology* **29**, 959–962.

Kim K. H. and McMurtry G. M. (1991) Radial growth-rates and Pb-210 ages of hydrothermal massive sulfides from the Juan de Fuca Ridge. *Earth Planet. Sci. Lett.* **104**, 299–314.

Konnerup-Madsen J. (1995) *Basic microthermometry observations on fluid inclusions in minerals – A working manual*. Geologisk Institut, Copenhagen.

Koski R. A., Jonasson I. R., Kadko D. C., Smith V. K. and Wong F. L. (1994) Compositions, growth mechanisms, and temporal relations of hydrothermal sulfide-sulfate-silica chimneys at the northern Cleft Segment, Juan de Fuca Ridge. *J. Geophys. Res. Solid Earth* **99**, 4813–4832.

Kristall B., Kelley D. S., Hannington M. D. and Delaney J. R. (2006) Growth history of a diffusely venting sulfide structure from the Juan de Fuca Ridge: A petrological and geochemical study. *Geochem. Geophys. Geosyst.* **7**.

Kumagai H., Nakamura K., Toki T., Morishita T., Okino K., Ishibashi J. I., Tsunogai U., Kawagucci S., Gamo T., Shibuya

T., Sawaguchi T., Neo N., Joshima M., Sato T. and Takai K. (2008) Geological background of the Kairei and Edmond hydrothermal fields along the Central Indian Ridge: implications of their vent fluids' distinct chemistry. *Geofluids* **8**, 239–251.

Kusakabe M., Mayeda S. and Nakamura E. (1990) S, O and Sr isotope systematic of active vent materials from the Mariana Backarc Basin spreading axis at 18 °N. *Earth Planet. Sci. Lett.* **100**, 275–282.

Larson B. I., Lilley M. D. and Olson E. J. (2009) Parameters of subsurface brines and hydrothermal processes 12–15 months after the 1999 magmatic event at the Main Endeavor Field as inferred from in situ time series measurements of chloride and temperature. *J. Geophys. Res. Solid Earth* **114**, 1–18.

Li S. W., Xu J. H. and Luo G. S. (2007) Control of crystal morphology through supersaturation ratio and mixing conditions. *J. Cryst. Growth* **304**, 219–224.

Lilley M. D., Butterfield D. A., Lupton J. E. and Olson E. J. (2003) Magmatic events can produce rapid changes in hydrothermal vent chemistry. *Nature* **422**, 878–881.

Lilley M. D., Butterfield D. A., Olson E. J., Lupton J. E., Macko S. A. and McDuff R. E. (1993) Anomalous CH4 and NH4+ concentrations at an unsedimented mid-ocean-ridge hydrothermal system. *Nature* **364**, 45–47.

McCollom T. M. and Shock E. L. (1997) Geochemical constraints on chemolithoautotrophic metabolism by microorganisms in seafloor hydrothermal systems. *Geochim. Cosmochim. Acta* **61**, 4375–4391.

Mills R., Teagle D. and Tivey M. (1998) Fluid mixing and anhydrite precipitation within the TAG mound. In *Proceedings of the Ocean Drilling Program, Scientific Results*, Vol. 158 (eds. P. Herzig, S. Humphris, D. Miller and R. Zierenberg). Ocean Drilling Program, College Station, TX, pp. 119–127.

Mills R. A. and Elderfield H. (1995) Rare-earth element geochemistry of hydrothermal deposits from the active TAG mound, 26° N Mid-Atlantic Ridge. *Geochim. Cosmochim. Acta* **59**, 3511–3524.

Nelson B. K. (1995) Fluid-flow in subduction zones – evidence from Nd and Sr-isotope variations in metabasalts of the Franciscan Complex, California. *Contrib. Mineral. Petrol.* **119**, 247–262.

Proskurowski G., Lilley M. D. and Brown T. A. (2004) Isotopic evidence of magmatism and seawater bicarbonate removal at the endeavour hydrothermal system. *Earth Planet. Sci. Lett.* **225**, 53–61.

Rasmussen B. (2000) Filamentous microfossils in a 3,235-million-year-old volcanogenic massive sulphide deposit. *Nature* **405**, 676–679.

Riddihough R. (1984) Recent movements of the Juan-de-Fuca plate system. *J. Geophys. Res.* **89**, 6980–6994.

Robigou V., Delaney J. R. and Stakes D. S. (1993) Large massive sulfide deposits in a newly discovered active hydrothermal system, the Highrise Field, Endeavour Segment, Juan-de-Fuca Ridge. *Geophys. Res. Lett.* **20**, 1887–1890.

Roedder E. (1984) Fluid inclusions. *Rev. Mineral.* **12**, 1.

Ruiz-Agudo C., Putnis C. V., Ruiz-Agudo E. and Putnis A. (2015) The influence of pH on barite nucleation and growth. *Chem. Geol.* **391**, 7–18.

Sasaki N. and Minato H. (1983) Effect of the degree of supersaturation upon apparent partition coefficients of lead and strontium ions between BaSO4 and aqueous solution. *Mineral. J.* **11**, 365–381.

Seewald J., Cruse A. and Saccocia P. (2003) Aqueous volatiles in hydrothermal fluids from Main Endeavour Field, northern Juan de Fuca Ridge: temporal variability following earthquake activity. *Earth Planet. Sci. Lett.* **216**, 575–590.

Seyfried W. E., Seewald J. S., Berndt M. E., Ding K. and Foustoukos D. I. (2003) Chemistry of hydrothermal vent fluids from the Main Endeavour Field, northern Juan de Fuca Ridge: Geochemical controls in the aftermath of June 1999 seismic events. *J. Geophys. Res. Solid Earth* **108**, 1–23.

Shikazono N. (1994) Precipitation mechanisms of barite in sulfate-sulfide deposits in back-arc basins. *Geochim. Cosmochim. Acta* **58**, 2203–2213.

Shikazono N., Kawabe H. and Ogawa Y. (2012) Interpretation of mineral zoning in submarine hydrothermal ore deposits in terms of coupled fluid flow-precipitation kinetics model. *Resour. Geol.* **62**, 352–368.

Teagle D. A. H., Alt J. C., Chiba H., Humphris S. E. and Halliday A. N. (1998) Strontium and oxygen isotopic constraints on fluid mixing, alteration and mineralization in the TAG hydrothermal deposit. *Chem. Geol.* **149**, 1–24.

Tivey M. K. (1995) The influence of hydrothermal fluid composition and advection rates on black smoker chimney mineralogy – Insights from modeling transport and reaction. *Geochim. Cosmochim. Acta* **59**, 1933–1949.

Tivey M. K. (2004) Environmental conditions within active seafloor vent structures: sensitivity to vent fluid composition and fluid flow. In *Subseafloor Biosphere at Mid-Ocean Ridges, Geophysical Monograph Series, No. 144* (eds. W. Wilcock, C. Cary, E. DeLong, D. Kelley and J. Baross). American Geophysical Union, Washington, DC, pp. 137–152.

Tivey M. K. and Delaney J. R. (1986) Growth of large sulfide structures on the Endeavour Segment of the Juan-de-Fuca Ridge. *Earth Planet. Sci. Lett.* **77**, 303–317.

Tivey M. K. and McDuff R. E. (1990) Mineral precipitation in the walls of black smoker chimneys – A quantitative model of transport and chemical-reaction. *J. Geophys. Res. Solid Earth Planets* **95**, 12617–12637.

Tivey M. K., Olson L. O., Miller V. W. and Light R. D. (1990) Temperature-measurements during initiation and growth of a black smoker chimney. *Nature* **346**, 51–54.

Tivey M. K., Stakes D. S., Cook T. L., Hannington M. D. and Petersen S. (1999) A model for growth of steep-sided vent structures on the Endeavour Segment of the Juan de Fuca Ridge: results of a petrologic and geochemical study. *J. Geophys. Res. Solid Earth* **104**, 22859–22883.

Turcotte D. (1997) *Fractals and Chaos in Geology and Geophysics*. Cornell University, New York.

Turekian K. K. (1968) *Oceans*. Prentice-Hall, Englewood Cliffs, NJ.

Ulrich M. and Bodnar R. (1988) Systematics of stretching of fluid inclusions; II, Barite at 1 atm confining pressure. *Econ. Geol.* **83**, 1037–1046.

Vearncombe S., Barley M. E., Groves D. I., McNaughton N. J., Mikucki E. J. and Vearncombe J. R. (1995) 3.26 Ga Black smoker-type mineralization in the Strelley Belt, Pilbara-Craton, Western-Australia. *J. Geol. Soc.* **152**, 587–590.

Von Damm K. L. (1990) Seafloor hydrothermal activity – Black smoker chemistry and chimneys. *Annu. Rev. Earth Planet. Sci.* **18**, 173–204.

Widanagamage I. H., Schauble E. A., Scher H. D. and Griffith E. M. (2014) Stable strontium isotope fractionation in synthetic barite. *Geochim. Cosmochim. Acta* **147**, 58–75.

Wolery T. J. (1992) *EQ3NR, A Computer Program for Geochemical Aqueous Speciation-Solubility Calculations: Theoretical Manual, User's Guide, and Related Documentation (Version 7.0)*. Lawrence Livermore Natl. Lab, Livermore, California.

Wolery T. J. and Daveler S. A. (1992) *EQ6, A Computer Program for Reaction Path Modeling of Aqueous Geochemical Systems:*

Theoretical Manual, User's Guide, and Related Documentation (Version 7.0). Lawrence Livermore Natl. Lab, Livermore, California.

Yao H.-Q., Zhou H.-Y., Peng X.-T., Bao S.-X., Wu Z.-J., Li J.-T., Sun Z.-L., Chen Z.-Q., Li J.-W. and Chen G.-Q. (2009) Metal sources of black smoker chimneys, Endeavour Segment, Juan de Fuca Ridge: Pb isotope constraints. *Appl. Geochem.* **24**, 1971–1977.

You C. F., Butterfield D. A., Spivack A. J., Gieskes J. M., Gamo T. and Campbell A. J. (1994) Boron and halide systematics in submarine hydrothermal systems – Effects of phase-separation and sedimentary contributions. *Earth Planet. Sci. Lett.* **123**, 227–238.

Associate editor: Weidong Sun

SUPPLEMENTARY INFORMATION

Table S1: Bulk geochemical analyses of sulfide samples from hydrothermal deposits along the Endeavour Segment.

Sample	**Ba (wt. %)**	**CaO (wt. %)**	**Sr (wt. %)**	**Sr/Ba**
Analysis	INAA	ICP-ES	ICP-ES	
Detection Limit	0.005 wt.%	0.01 wt.%	0.001 wt.%	
ALV1417-1a b2	8.800	0.14	0.2000	0.023
ALV1417-1b b2	0.029	0.11	0.0011	0.038
ALV1417-1b b8	1.200	0.16	0.0410	0.034
ALV1417-1c b2	8.900	0.10	0.2200	0.025
ALV1417-1c b22	0.470	0.07	0.0091	0.019
ALV1417-1d b7	0.003	0.04	0.0011	0.393
ALV1417-1e	0.002	0.06	b.d.	
ALV1417-2a b5	2.100	0.12	0.0540	0.026
ALV1417-2b	0.016	0.06	0.0014	0.088
ALV1417-5a b11	0.002	0.29	b.d.	
ALV1417-5b b12	0.004	0.30	b.d.	
ALV1417-5c b13	0.003	0.29	0.0024	0.800
ALV1417-5d b14	0.008	0.27	0.0024	0.300
ALV1417-c b9	0.011	0.07	b.d.	
ALV1418-1d b2	0.007	0.06	b.d.	
ALV1418-1d b5	1.400	0.04	0.0210	0.015
ALV1418-1e b2	37.00	0.31	0.6900	0.019
ALV1418-3a	1.400	0.04	0.0210	0.015
ALV1418-6b b9	1.300	0.12		
ALV1418-8b b6	0.012	0.06	0.0001	0.008
ALV1419-1a b2	1.300	0.13	0.0470	0.036
ALV1419-1b b3	0.021	0.03	0.0011	0.052
ALV1419-1c b2	37.00	0.32	0.6900	0.019
ALV1419-1d b3	39.00	0.29	0.7400	0.019
ALV1419-1d b31	22.00	0.23	0.4300	0.020
ALV1419-1h b4	32.000	0.31	0.6900	0.022
ALV1419-2 b10	0.008	0.01	b.d.	
ALV1439	0.300	0.33	0.0193	0.064
ALV1445-3A		1.52	b.d.	
ALV1445-3B		8.36	b.d.	
ALV1445-3C		6.80	b.d.	
ALV1445-3D		3.35	b.d.	
ALV1445-7	0.250	0.03	0.0139	0.056
ALV1447-1		10.30	0.0881	
ALV1451-1	0.290	0.33	0.0205	0.071
ALV1452-1A	12.00	0.25	0.8230	0.069
ALV1452-2	8.500	0.16	0.3880	0.046
ALV2057	0.340	0.03	0.0155	0.046
ALV2061-2A	0.022	5.83	0.0399	1.814
ALV2061-2B	0.034	1.04	0.0074	0.218
ALV2063-1B	0.094	0.41	0.0085	0.090
ALV2066-3	0.016	17.20	0.1140	7.125
ALV2066-4A	0.520	0.28	0.0251	0.048
ALV2066-4B	0.003	0.23	0.0015	0.600
ALV2066-5	0.003	34.10	0.0856	34.240
ALV2066-6	0.003	0.16	0.0022	0.880
ALV2068-1	23.00	0.34	1.2800	0.056
ALV2072-1B	7.500	0.19	0.6440	0.086
ALV2072-7	5.000	0.15	0.3170	0.063
ALV2073-1	0.110	25.80	0.1970	1.791
ALV2116-4b-1		27.10	0.7390	
ALV2116-R3-H1		0.27	1.3300	
ALV2116-R4a-4		4.41	1.1100	
ALV2404-1	0.003	1.00	0.0083	3.320
ALV2404-3A	0.003	0.02	0.0005	0.200

Sample	**Ba (wt. %)**	**CaO (wt. %)**	**Sr (wt. %)**	**Sr/Ba**
Analysis	INAA	ICP-ES	ICP-ES	
Detection Limit	0.005 wt.%	0.01 wt.%	0.001 wt.%	
ALV2404-3B	0.280	0.07	0.0130	0.046
ALV2404-4	0.890	0.03	0.0357	0.040
ALV2406-1A	0.120	0.18	0.0107	0.089
ALV2406-1B	0.003	8.71	0.0375	15.000
ALV2408-1A	1.650	0.11	0.0813	0.049
ALV2408-1B	0.003	1.62	0.0125	5.000
ALV2409-1B	0.082	0.04	0.0019	0.023
ALV2411-1A	0.035	30.70	0.2950	8.429
ALV2411-2	0.003	0.11	0.0005	0.200
ALV2412-1	0.220	0.03		
ALV2413-2	0.003	0.09	0.0005	0.200
ALV2414-1	0.078	5.91	0.0462	0.592
ALV2415-1D(1)	0.870	0.08	0.0443	0.051
ALV2415-1D(2)	0.003	0.10	0.0005	0.200
ALV2415-1D(3)	2.700	0.10	0.1300	0.048
ALV2418-1	0.010	0.01	0.0005	0.050
ALV2419-1	0.023	0.04	0.0005	0.022
ALV2419-2	0.023	10.80	0.0795	3.457
ALV2420-1B	0.061	1.18	0.0105	0.172
ALV2420A	0.370	0.27	0.0241	0.065
ALV2420B	0.015	27.70	0.1820	12.133
ALV2448-1	0.003	4.94	0.0332	13.280
ALV2449-1	1.600	0.09	0.0290	0.018
ALV2450-2	0.240	0.05	0.0065	0.027
ALV2450-3b (crust)		0.06	0.0370	
ALV2451-1	0.028	1.46	0.0092	0.329
ALV2452-1	0.015	1.15	0.0097	0.647
ALV2452-2	1.650	0.03	0.0373	0.023
ALV2453-1A	0.044	0.07	0.0015	0.034
ALV2453-1B	0.015	1.11	0.0081	0.540
ALV2453-2 (puffer)	0.003	0.51	0.0032	1.280
ALV2453-3	0.010	0.06	0.0010	0.100
ALV2460 B	0.440		0.0010	0.002
ALV2460 E	0.080		0.0010	0.013
ALV2460-R2-14a	2.600	0.06	0.0440	0.017
ALV2460-R2-14b	0.580	0.04	0.0065	0.011
ALV2460-R2-15	0.860	0.07	0.0250	0.029
ALV2460-R3-3	1.200	0.10	0.0400	0.033
ALV2460-R3-3c	0.980	0.17	0.0350	0.036
ALV2460-R3-5	0.750	6.45	0.0730	0.097
ALV2460-R4-1c	0.019	0.05	0.0010	0.053
ALV2460-R5	0.041	26.27	0.2100	5.122
ALV2460-R5P1C		31.90	0.2440	
ALV2460-R5P2C		38.70	0.2700	
ALV2460-R5P3B-D		35.70	0.2790	
ALV2461 A	8.870		0.2800	0.032
ALV2461 E	0.630		0.0215	0.034
ALV2461-R10-2		0.08	0.0017	
ALV2461-R10b2	0.015	0.06	0.0010	0.067
ALV2461-R11-9	1.200	1.19	0.0380	0.032
ALV2461-R12-2	0.280	1.78	0.0200	0.071
ALV2461-R13 TIP	4.600	0.21	0.1000	0.022
ALV2461-R13/1	0.280	0.06	0.0120	0.043
ALV2461-R13/2	0.320	0.04	0.0110	0.034
ALV2461-R13/3	1.100	0.07	0.0280	0.025
ALV2461-R13/4	5.600	0.20	0.0950	0.017
ALV2461-R13-4-BOT	0.970	0.06	0.0350	0.036
ALV2461-R1b2	0.730	0.07	0.0290	0.040
ALV2461-R-3		0.07	0.0334	
ALV2461-R-3-2		0.01	0.0005	
ALV2461-R3c1	0.008	0.04	0.0160	2.000
ALV2461-R4-2		0.03	0.0005	
ALV2461-R4d	0.007	0.05	0.0010	0.143

Sample	**Ba (wt. %)**	**CaO (wt. %)**	**Sr (wt. %)**	**Sr/Ba**
Analysis	INAA	ICP-ES	ICP-ES	
Detection Limit	0.005 wt.%	0.01 wt.%	0.001 wt.%	
ALV2461-R6-4	1.500	0.22	0.0370	0.025
ALV2461-R7c2	1.700	0.10	0.0440	0.026
ALV2461-R8-3	0.025	22.92	0.2200	8.800
ALV2462 A1	4.070		0.1480	0.036
ALV2462-R1a	0.760	0.44	0.0240	0.032
ALV2462-R1b	0.041	26.49	0.2500	6.098
ALV2462-R1c	0.620	0.13	0.0210	0.034
ALV2462-R6-1d2	0.070	0.09	0.0028	0.040
ALV2462-R7-1b	0.600	4.26	0.0420	0.070
ALV2463 A	0.010		0.0010	0.100
ALV2463 F	0.003		0.0010	0.400
ALV2463-R1-2	0.010	0.10	0.0010	0.100
ALV2463-R2-1a	0.007	0.09	0.0010	0.143
ALV2463-R2-3		0.02	0.0005	
ALV2463-R2P2B			0.0005	
ALV2463-R3-3	22.00	0.20	0.3650	0.017
ALV2463-R3-misc			b.d.	
ALV2463-R4-pc	26.00	0.22	0.5700	0.022
ALV2463-R5c2		0.04	0.0715	
ALV2463-R5c3	1.800	0.09	0.0290	0.016
ALV2463-R6-misc	0.003	0.04	0.0010	0.400
ALV2463-R7-6B	0.220	0.01	b.d.	
ALV2463-R7-6C	10.70	0.45	0.3610	0.034
ALV2463-R7-6G	30.50	0.01	0.8900	0.029
ALV2464 B	0.003		0.0010	0.400
ALV2464 F-V	0.010		0.0010	0.100
ALV2464-R4		0.11	0.1290	
ALV2464-R5-3	1.700	0.08	0.0380	0.022
ALV2464-R6-2c	0.620	0.19	0.0250	0.040
ALV2464-R6P1C		0.10	0.1200	
ALV2464-R6-pc		0.09	0.0683	
ALV2464-R8-1b	1.100	0.13	0.0370	0.034
ALV2465-R1-6c	0.760	0.12	0.0210	0.028
ALV2465-R1P1A		14.80	0.1270	
ALV2465-R2-1e	0.008	5.50	0.0460	5.750
ALV2465-R2-2a2	0.035	18.56	0.1600	4.571
ALV2465-R2-2d2	0.094	25.49	0.2000	2.128
ALV2465-R2-3b	0.060	11.85	0.1100	1.833
ALV2465-R2A	0.003	8.93	0.0700	28.000
ALV2465-R2b	0.039	1.48	0.0100	0.256
ALV2465-R3-2a	0.029	21.35	0.2000	6.897
ALV2466 A	0.890	0.06	0.0311	0.035
ALV2466 E	1.130	0.04	0.0282	0.025
ALV2466-b	0.170	2.46	0.0220	0.129
ALV2466-c	0.200	0.06	0.0080	0.040
ALV2466-R1		0.02	0.0005	
ALV2466-R1-4b	0.007	0.09	0.0028	0.400
ALV2466-R1P3B2		0.01	0.0005	
ALV2466-R3	0.330	0.04	0.0081	0.025
ALV2466-R3-1b1	0.450	0.07	0.0120	0.027
ALV2466-R3-1b2	0.370	0.06	0.0115	0.031
ALV2466-R4	0.019	9.71	0.0650	3.421
ALV2466-R4-misc			b.d.	
ALV2466-R5-8/1	0.430	0.12	0.0190	0.044
ALV2466-R5-8/2	0.015	1.78	0.0120	0.800
ALV2466-R5-8/3	0.020	0.06	0.0010	0.050
ALV2466-R5-8/4	0.610	0.09	0.0190	0.031
ALV2467-R1		16.60	0.2190	
ALV2467-R1-14d	0.069	2.46	0.0230	0.333
ALV2467-R1-1b3	0.054	0.65	0.0065	0.120
ALV2467-R1exc	0.040	20.85	0.1900	4.750
ALV2467-R2	23.10	0.07	0.4560	0.020
ALV2467-R3	26.50	0.15	0.2000	0.008

Sample	Ba (wt. %)	CaO (wt. %)	Sr (wt. %)	Sr/Ba
Analysis	INAA	ICP-ES	ICP-ES	
Detection Limit	0.005 wt.%	0.01 wt.%	0.001 wt.%	
ALV2467-R4-misc	0.013	0.04	0.0010	0.077
ALV2467-R9	8.650	0.01	0.2240	0.026
ALV2927-A	2.700	0.10	0.1190	0.044
ALV2927-B		0.07	0.0005	
ALV2929	0.034	29.00	0.2300	6.765
ALV2936-A	0.260	0.05	0.0146	0.056
ALV2936-B	1.150	0.08	0.0591	0.051
ALV2996MEF	0.003	0.01	0.0005	0.200
ALV2997AH	0.041	27.00	0.2090	5.098
ALV2998-A	0.003	0.04	0.0005	0.200
ALV2998-B	0.550	0.39	0.0133	0.024
ALV2998-Salut (1of2)	0.150	6.09	0.0557	0.371
ALV2998-Salut (2of2)	0.220	6.44	0.0630	0.286
ALV3000C	1.700	0.08	0.0365	0.021
ALV3000-GrendleA	0.180	0.04	0.0098	0.054
ALV3000-SpireB	2.200	0.11	0.0443	0.020
ALV3003	0.870	0.42	0.0204	0.023
ALV3005A	0.320	11.70	0.0921	0.288
ALV3005B	0.036	0.02	0.0023	0.064
ALV3569-R1-A	0.026	11.20	0.0688	2.646
ALV3569-R1-B	0.560	0.21	0.0156	0.028
ALV3570-MISC(A)		10.80	0.0872	
ALV3570-MISC(B)		2.16	0.0147	
ALV3570-R2	0.480	2.99	0.0321	0.067
ALV3570-R2D	0.120	20.00	0.1620	1.350
ALV3572-R1	0.150	0.03	0.0027	0.018
ALV3581-R-1	33.00	0.67	0.9250	0.028
ALV3581-R-2	0.073	22.60	0.1860	2.548
ALV3586-R-1A	0.003	0.23	0.0022	0.880
ALV3586-R-1B	0.017	0.32	0.0029	0.171
ALV3587-R-1	6.100	0.07	0.1150	0.019
ALV3587-R-2	0.026	29.10	0.2580	9.923
ALV3588-A	0.200	10.30	0.0804	0.402
ALV3588-B (R1)	0.029	32.40	0.2780	9.586
ALV3588-R2A	0.580	6.28	0.0957	0.165
ALV3588-R2B	0.930	0.03	0.0337	0.036
ALV3589-R2	11.00	0.17	0.5570	0.051
ALV3609-01A	0.003	23.20	0.1490	59.600
ALV3612-01	0.022	26.00	0.2040	9.273
ALV3616-03	0.130	0.02	0.0056	0.043
ALV3616-A	0.790	0.05	0.0256	0.032
ALV3616-B	4.100	0.09	0.0975	0.024
ALV3619-01	0.003	0.64	0.0046	1.840
ALV3622	0.003	0.01	b.d.	
ALV3622-01A	5.400	0.21	0.1990	0.037
ALV3622-01F	0.040	0.01	0.0027	0.068
ALV3622-1	0.003	0.01	0.0011	0.440
ALV3623-02	0.015	0.01	0.0005	0.033
ALV4438-1635	0.763	0.01	0.0395	0.052
ALV4438-1816	0.308	4.88	0.0566	0.184
ALV4438-1816 (inner)	0.350	0.10	0.0289	0.083
ALV4438-1816 (outer)	0.625	0.01	0.0440	0.070
ALV4438-2132	0.003	0.01	0.0025	1.000
ALV4441-1912	0.500	0.01	0.0336	0.067
ALV4441-2135	0.019	3.46	0.0188	0.989
ALV4446-1628	1.250	0.07	0.0631	0.050
ALV4446-1735	1.190	15.67	0.1580	0.133
ALV4448-2211	0.863	0.01	0.0429	0.050
ALV4449-1630	2.130	0.24	0.1510	0.071
ALV4449-1938	0.025	37.21	0.1970	7.880
ALV4449-1938 (inner)	0.054	39.45	0.1870	3.463
ALV4449-1938 (outer)	0.033	7.82	0.0424	1.285
ALV4450-1538	0.077	38.89	0.2210	2.870

Sample	**Ba (wt. %)**	**CaO (wt. %)**	**Sr (wt. %)**	**Sr/Ba**
Analysis	INAA	ICP-ES	ICP-ES	
Detection Limit	0.005 wt.%	0.01 wt.%	0.001 wt.%	
ALV4450-1538 (inner)	0.040	24.90	0.1260	3.150
ALV4450-1829	22.10	0.39	1.0000	0.045
ALV4451-1725	0.208	38.05	0.2260	1.087
ALV4452-1706	0.377	10.23	0.0796	0.211
ALV4517-1703	0.468	0.01	0.0422	0.090
ALV4517-1718	0.702	0.01	0.0574	0.082
ALV4518-1836	0.025	38.05	0.2370	9.480
ALV4518-1836 (inner)	0.020	29.10	0.1690	8.450
ALV4518-1836 (outer)	0.013	36.09	0.2270	17.462
ALV4525-0134	0.713	0.06	0.0598	0.084
ALV-Grotto-Sep95	0.003	0.01	0.0005	0.200
D264-R2	0.003	0.01	0.0006	0.240
D264-R22	6.120	0.17	0.3630	0.059
D264-R3	0.666	0.07	0.0423	0.064
D264-R5	2.610	0.18	0.1950	0.075
D264-R6	0.035	0.01	0.0048	0.137
D265-R2	0.003	0.04	0.0011	0.440
D265-R3	0.003	0.04	0.0004	0.160
D265-R4	0.003	0.10	0.0011	0.440
D265-R8	2.250	0.18	0.1190	0.053
D266-R4	9.900	0.11	0.2330	0.024
D266-R5	0.477	0.13	0.0250	0.052
D266-R6	0.003	0.07	0.0074	2.960
D266-R8	0.003	0.07	0.0015	0.600
D266-R9	2.520	0.35	0.1460	0.058
Endv-1. vent	0.007		b.d.	
FINN-CPY	0.750	0.07	0.0293	0.039
FINN-SPH	4.900	2.00	b.d.	
FINN-ZN Silica		1.69	0.1910	
G2 mucus	0.003	1.00	0.0050	2.000
HYS 270-1	0.003	0.04	0.0005	0.200
HYS 278-14	0.003	0.02	0.0005	0.200
HYS 278-3	0.011	0.26	0.0021	0.191
HYS 278-4	1.300	0.04	0.0438	0.034
HYS 278-9	0.003	0.01	0.0005	0.200
HYS 280-16	1.100	0.01	0.0537	0.049
HYS-278-01	0.980	0.04	0.0227	0.023
HYS-278-02a	1.200	0.06	0.0350	0.029
HYS-278-02b	0.850	0.04	0.0406	0.048
HYS-278-09a	0.003	0.01	0.0006	0.240
HYS-278-09b	0.003	0.01	0.0003	0.120
HYS-278-10	0.057	0.01	0.0016	0.028
HYS-278-11	0.003	0.01	0.0005	0.200
HYS-278-14a	0.003	0.01	0.0002	0.080
HYS-278-14b	0.003	0.01	0.0002	0.080
HYS-278-16	2.800	0.04	0.0238	0.009
HYS-347-01	1.800	0.08	0.0167	0.009
HYS-347-02	0.010	1.07	0.0105	1.050
HYS-350-01	0.240	1.13	0.0162	0.068
HYS-350-02	0.017	1.63	0.0161	0.947
HYS-350-02(a)	25.00	0.27	0.0990	0.004
HYS-355-01	0.047	0.11	0.0006	0.013
HYS-355-02	0.003	0.03	0.0002	0.080
HYS-355-B	4.800	5.83	0.0761	0.016
HYS-356-01A	0.048	2.73	0.0226	0.471
HYS-356-01B	0.003	1.06	0.0074	2.960
HYS-356-02A	0.045	16.60	0.1648	3.662
HYS-363-01A	0.015	1.47	0.0141	0.940
HYS-363-01B	11.00	0.40	0.0226	0.002
HYS-363-01C	0.007	0.33	0.0033	0.508
J2-52-1	0.039	5.84	0.0412	1.056
J2-59-1	0.044	37.20	0.2730	6.205
J2-59-2	0.110	3.76	0.0336	0.305

Sample	**Ba (wt. %)**	**CaO (wt. %)**	**Sr (wt. %)**	**Sr/Ba**
Analysis	INAA	ICP-ES	ICP-ES	
Detection Limit	0.005 wt.%	0.01 wt.%	0.001 wt.%	
J2-59-4 Misc	0.990	0.05	0.0561	0.057
J2-59-4D	0.003	0.04	0.0005	0.200
Pisces 1B	0.003	0.43	0.0149	5.960
R1348-1007-Ba	0.000	0.03	0.0129	180.926
R1348-1007-S	0.002	0.08	0.0009	0.390
R507-9	0.047	37.80	0.2490	5.298
TIVEY MISC-1	0.875	0.09	0.0971	0.111
TIVEY MISC-2	33.00	0.15	0.7160	0.022
TIVEY MISC-3	0.008	0.03	0.0005	0.063
TIVEY MISC-4	0.580	0.07	0.0496	0.086
TIVEY MISC-5	0.170	7.22	0.0657	0.386
TIVEY MISC-6	0.100	0.01	0.0035	0.035
TIVEY MISC-7	1.100	0.02	0.0444	0.040
TT 170-66D 1B	0.380	0.07	0.0140	0.037
TT 170-66D AIS 9T 1	0.030	0.01	0.0011	0.037
TT 170-66D AIS 9T 2	0.003	0.01	0.0010	0.400
TT 170-66D AIS Inner 1	0.048	0.02	0.0019	0.040
TT 170-66D AIS Inner 2	0.042	0.01	0.0016	0.038
TT 170-66D AIS Slab 1	0.049	0.01	0.0018	0.037
TT 170-66D AIS Slab 2	0.051	0.01	0.0016	0.031
TT 170-66D B112A	0.025	0.01	0.0005	0.020
TT 170-66D B19-B2	0.021	0.01	0.0015	0.071
TT 170-66D B1-B2	0.003	0.01	0.0005	0.200
TT 170-66D B30-A	0.060	0.01	0.0027	0.045
TT 170-66D B9-B	0.003	0.03	0.0013	0.520
TT 170-66D EXIT CH 1	0.026	0.02	0.0005	0.019
TT 170-66D EXIT CH 2	b.d.	0.13	0.0005	
TT 170-66D R2	0.003	0.01	0.0005	0.200

b.d.: Below detection limits

Table S2: Relative cation concentrations in barite from electron microprobe analysis (normalized to total Ba+Sr+Ca)

Sample	Analysis	Ba (%)	Sr (%)	Ca (%)
ALV2072-7	1	86.7	6.7	6.7
	2	86.7	6.7	6.7
	3	84.4	8.9	6.7
	4	84.4	8.9	6.7
	5	88.9	6.7	4.4
	6	86.7	6.7	6.7
	7	84.4	6.7	6.7
ALV3589-R2	1	95.5	4.6	b.d.
	2	97.7	2.3	b.d.
	3	100.0	b.d.	b.d.
	4	95.5	4.6	b.d.
	5	93.0	7.0	b.d.
	6	95.4	4.7	b.d.
	7	97.7	2.3	b.d.
ALV2467-R2	1	95.5	4.6	n.d.
	2	90.9	9.1	n.d.
	3	97.7	2.3	n.d.
	4	95.4	4.7	n.d.
	5	97.7	2.3	n.d.
	6	93.2	6.8	n.d.
ALV2068-1	1	97.7	2.3	b.d.
	2	78.3	10.9	10.9
	3	80.0	17.8	2.2
	4	88.6	9.1	2.3
ALV2467-R3	1	95.5	4.6	b.d.
	2	93.0	7.0	b.d.
	3	97.7	2.3	b.d.
	4	97.7	2.3	b.d.
Tivey Misc-2	1	97.7	2.3	b.d.
	2	95.5	4.6	b.d.
	3	95.5	4.6	b.d.
	4	97.6	2.4	b.d.
	5	97.7	2.3	b.d.
	6	97.7	2.3	b.d.
ALV2464-R4	1	90.9	6.8	2.3
	2	97.7	2.3	b.d
	3	82.2	13.3	4.4
	4	95.5	4.6	b.d.
	5	88.6	11.4	b.d.
	6	100.0	b.d.	b.d.
	7	95.4	4.7	b.d.

b.d. = below detection limits, n.d. = not determined

Figure S1: Electron microprobe backscatter images showing locations of analyses reported in table S1.

ALV2072-7:

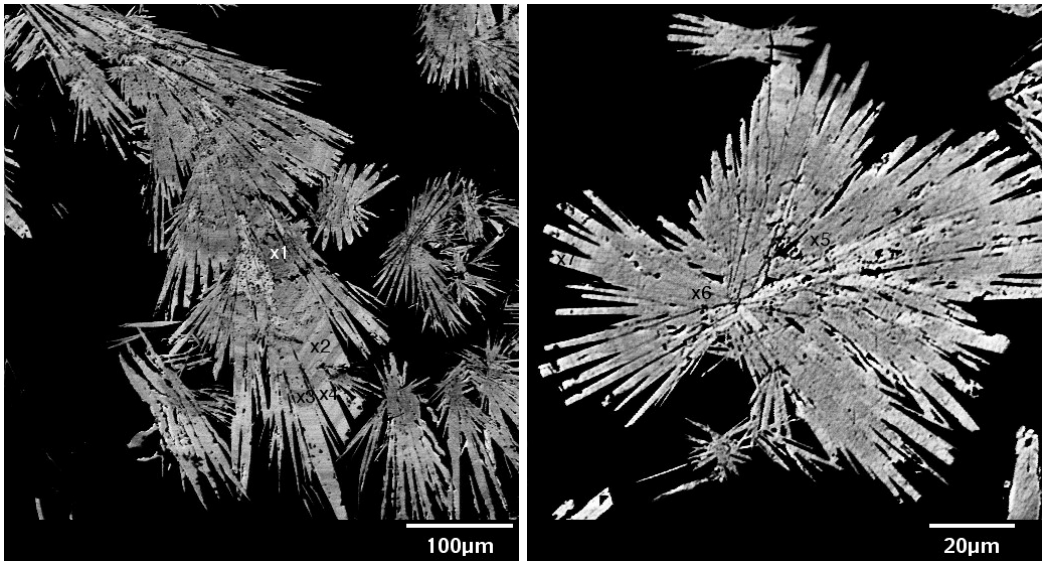

ALV3589-R2:

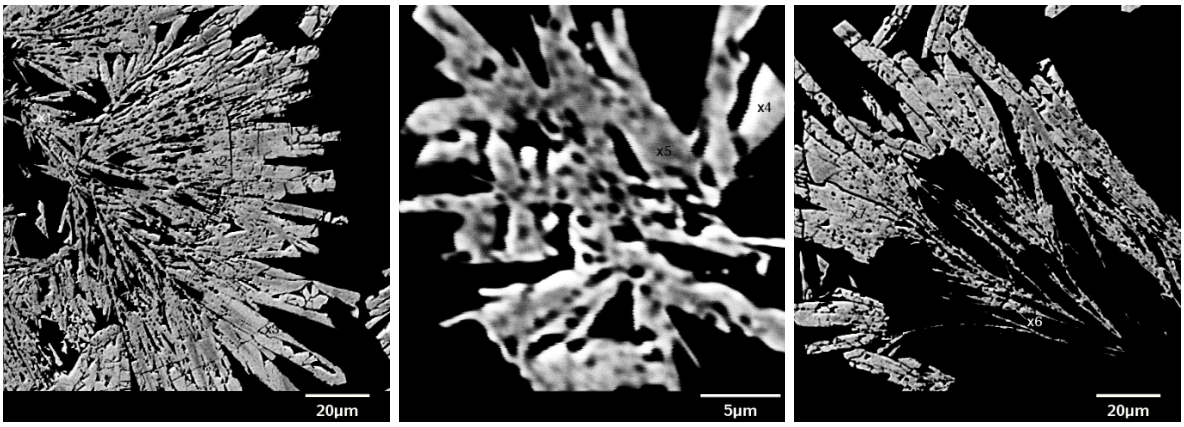

ALV2467-R2:

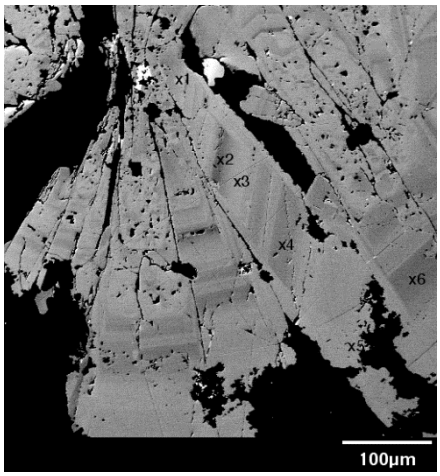

ALV2068-1:

Figure S1 (cont.):

ALV2467-R3:

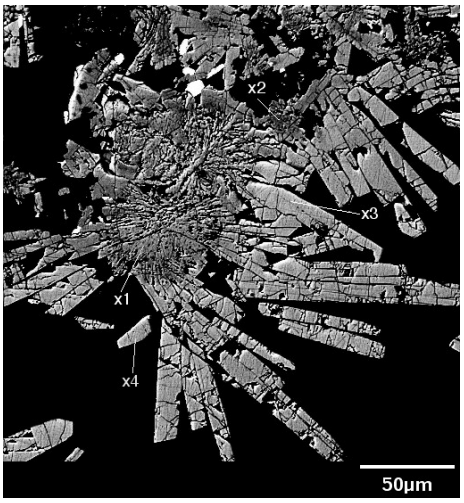

Tivey Misc-2:

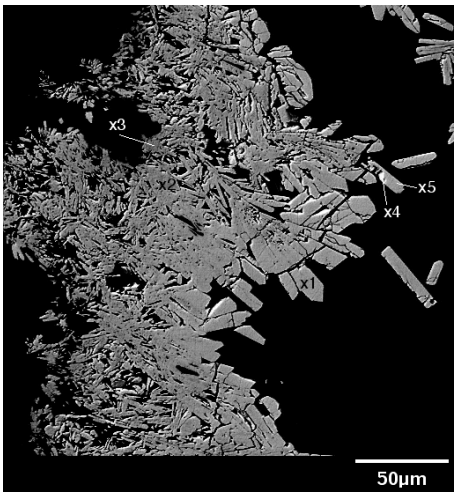

ALV 2464-R4:

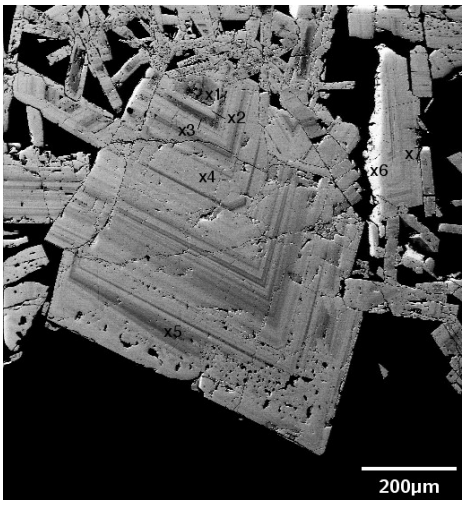

Table S3: Laser ablation ICP-MS trace element results for ALV2467-R2. Analytical lines correspond to locations in Figure 5C.

	Li(7) Li µg/g	Be(9) Be µg/g	B(11) B µg/g	Na(23) Na µg/g	Mg(24) Mg µg/g	Al(27) Al µg/g	P(31) P µg/g	S(33) S µg/g	S(34) S µg/g	K(39) K µg/g	Ca(43) Ca µg/g	Ca(44) Ca µg/g	Sc(45) Sc µg/g	Ti(49) Ti µg/g	V(51) V µg/g	Cr(52) Cr µg/g	Cr(53) Cr µg/g
barite line A (32µm, 2J/cm², 10Hz)	**n.d.**	**b.d.l.**	**1.8**	**9.8**	**b.d.l.**	**n.d.**	**55.4**	**126668**	**133354**	**234.6**	**5397.0**	**5079.3**	**b.d.l.**	**n.d.**	**n.d.**	**n.d.**	**n.d.**
2RSD %	---	---	93	76	---	---	29	10	9	15	17	13	---	---	---	---	---
barite line B (32µm, 2J/cm², 10Hz)	**n.d.**	**b.d.l.**	**5.5**	**19.3**	**1.6**	**n.d.**	**32.1**	**140552**	**145591**	**348.3**	**9269.2**	**8868.8**	**b.d.l.**	**2.9**	**b.d.l.**	**n.d.**	**b.d.l.**
2RSD %	---	---	67	48	57	---	43	10	10	8	9	5	---	74	---	---	---
barite line C (32µm, 2J/cm², 10Hz)	**b.d.l.**	**n.d.**	**n.d.**	**n.d.**	**b.d.l.**	**n.d.**	**32.8**	**128725**	**130201**	**142.4**	**4361.6**	**4298.8**	**n.d.**	**n.d.**	**b.d.l.**	**n.d.**	**n.d.**
2RSD %	---	---	---	---	---	---	41	9	9	9	15	6	---	---	---	---	---
barite line D (32µm, 2J/cm², 10Hz)	**n.d.**	**b.d.l.**	**n.d.**	**13.9**	**n.d.**	**b.d.l.**	**45.6**	**134767**	**141458**	**286.9**	**7947.6**	**8228.1**	**n.d.**	**n.d.**	**b.d.l.**	**b.d.l.**	**b.d.l.**
2RSD %	---	---	---	82	---	---	34	9	9	9	9	6	---	---	---	---	---
barite line E (32µm, 2J/cm², 10Hz)	**b.d.l.**	**b.d.l.**	**b.d.l.**	**n.d.**	**b.d.l.**	**n.d.**	**41.6**	**138672**	**145274**	**418.3**	**11842.3**	**11357.3**	**n.d.**	**2.6**	**b.d.l.**	**b.d.l.**	**n.d.**
2RSD %	---	---	---	---	---	---	30	9	10	8	8	4	---	91	---	---	---
barite line F (32µm, 2J/cm², 10Hz)	**b.d.l.**	**n.d.**	**n.d.**	**17.5**	**b.d.l.**	**b.d.l.**	**31.2**	**131443**	**133655**	**156.8**	**4556.1**	**4644.0**	**0.4**	**n.d.**	**b.d.l.**	**b.d.l.**	**n.d.**
2RSD %	---	---	---	82	---	---	44	9	9	14	19	7	94	---	---	---	---
barite line G (32µm, 2J/cm², 10Hz)	**b.d.l.**	**n.d.**	**n.d.**	**8.2**	**b.d.l.**	**1.6**	**38.6**	**121514**	**136006**	**42.3**	**2175.3**	**1970.8**	**b.d.l.**	**2.0**	**n.d.**	**n.d.**	**n.d.**
2RSD %	---	---	---	97	---	93	54	10	9	21	20	7	---	97	---	---	---
barite line H (32µm, 2J/cm², 10Hz)	**b.d.l.**	**b.d.l.**	**b.d.l.**	**n.d.**	**n.d.**	**b.d.l.**	**34.7**	**129821**	**142375**	**103.7**	**3963.8**	**3620.9**	**b.d.l.**	**2.7**	**n.d.**	**n.d.**	**n.d.**
2RSD %	---	---	---	---	---	---	41	10	9	18	13	11	---	96	---	---	---
Standards	Li µg/g	Be µg/g	B µg/g	Na µg/g	Mg µg/g	Al µg/g	P µg/g	S µg/g	S µg/g	K µg/g	Ca µg/g	Ca µg/g	Sc µg/g	Ti µg/g	V µg/g	Cr µg/g	Cr µg/g
NIST612	40	38	34	101635	68	10744	47	377	377	62	85049	85049	40	44	39	36	36
NIST610_611	468	476	350	99409	465	10320	413	575	575	464	81476	81476	455	452	450	408	408
PGE_Ni7b	-	-	-	-	-	-	-	392000	392000	-	-	-	-	-	-	-	-

	Mn(55) Mn µg/g	Fe(56) Fe µg/g	Fe(57) Fe µg/g	Co(59) Co µg/g	Ni(62) Ni µg/g	Cu(63) Cu µg/g	Zn(64) Zn µg/g	Ga(71) Ga µg/g	Ge(73) *Ge µg/g*	Ge(74) *Ge µg/g*	As(75) As µg/g	Se(77) Se µg/g	Rb(85) Rb µg/g	Sr(88) Sr µg/g	Zr(90) Zr µg/g	Nb(93) Nb µg/g	Mo(95) Mo µg/g
barite line A (32µm, 2J/cm², 10Hz)	**n.d.**	**22**	**b.d.l.**	**n.d.**	**b.d.l.**	**n.d.**	**8.6**	**n.d.**	*n.d.*	*b.d.l.*	**b.d.l.**	**b.d.l.**	**n.d.**	**17431.2**	**b.d.l.**	**b.d.l.**	**n.d.**
2RSD %	---	94	---	---	---	---	55	---	---	---	---	---	---	10	---	---	---
barite line B (32µm, 2J/cm², 10Hz)	**b.d.l.**	**n.d.**	**b.d.l.**	**b.d.l.**	**b.d.l.**	**n.d.**	**37.9**	**n.d.**	*n.d.*	*b.d.l.*	**n.d.**	**b.d.l.**	**n.d.**	**21860.6**	**b.d.l.**	**b.d.l.**	**b.d.l.**
2RSD %	---	---	---	---	---	---	52	---	---	---	---	---	---	7	---	---	---
barite line C (32µm, 2J/cm², 10Hz)	**b.d.l.**	**b.d.l.**	**n.d.**	**n.d.**	**n.d.**	**n.d.**	**9**	**n.d.**	*n.d.*	*n.d.*	**n.d.**	**n.d.**	**0.9**	**13567.1**	**n.d.**	**n.d.**	**n.d.**
2RSD %	---	---	---	---	---	---	65	---	---	---	---	---	88	7	---	---	---
barite line D (32µm, 2J/cm², 10Hz)	**b.d.l.**	**n.d.**	**n.d.**	**n.d.**	**n.d.**	**1**	**8.1**	**n.d.**	*b.d.l.*	*n.d.*	**n.d.**	**n.d.**	**n.d.**	**22805.8**	**b.d.l.**	**b.d.l.**	**b.d.l.**
2RSD %	---	---	---	---	---	81	84	---	---	---	---	---	---	8	---	---	---
barite line E (32µm, 2J/cm², 10Hz)	**n.d.**	**n.d.**	**n.d.**	**n.d.**	**b.d.l.**	**n.d.**	**15**	**0.5**	*n.d.*	*b.d.l.*	**1.8**	**b.d.l.**	**b.d.l.**	**25697.2**	**b.d.l.**	**b.d.l.**	**b.d.l.**
2RSD %	---	---	---	---	---	---	40	59	---	---	95	---	---	7	---	---	---
barite line F (32µm, 2J/cm², 10Hz)	**n.d.**	**n.d.**	**b.d.l.**	**b.d.l.**	**b.d.l.**	**n.d.**	**7**	**n.d.**	*n.d.*	*1.0*	**b.d.l.**	**b.d.l.**	**n.d.**	**14588.5**	**n.d.**	**b.d.l.**	**b.d.l.**
2RSD %	---	---	---	---	---	---	50	---	---	*97*	---	---	---	8	---	---	---
barite line G (32µm, 2J/cm², 10Hz)	**0.4**	**b.d.l.**	**b.d.l.**	**b.d.l.**	**n.d.**	**b.d.l.**	**n.d.**	**n.d.**	*b.d.l.*	*n.d.*	**b.d.l.**	**n.d.**	**b.d.l.**	**7557.5**	**b.d.l.**	**b.d.l.**	**n.d.**
2RSD %	89	---	---	---	---	---	---	---	---	---	---	---	---	8	---	---	---
barite line H (32µm, 2J/cm², 10Hz)	**n.d.**	**18**	**b.d.l.**	**b.d.l.**	**n.d.**	**b.d.l.**	**12**	**0.4**	*5.2*	*n.d.*	**n.d.**	**b.d.l.**	**n.d.**	**11649.9**	**b.d.l.**	**n.d.**	**b.d.l.**
2RSD %	---	84	---	---	---	---	51	73	*64*	---	---	---	---	10	---	---	---
Standards	Mn µg/g	Fe µg/g	Fe µg/g	Co µg/g	Ni µg/g	Cu µg/g	Zn µg/g	Ga µg/g	Ge µg/g	Ge µg/g	As µg/g	Se µg/g	Rb µg/g	Sr µg/g	Zr µg/g	Nb µg/g	Mo µg/g
NIST612	39	51	51	36	39	38	39	37	36	36	36	16	31	78	38	39	37
NIST610_611	444	458	458	410	459	441	460	433	447	447	325	138	426	516	448	465	417
PGE_Ni7b	-	568000	568000	-	47900	-	-	-	-	-	-	-	-	-	-	-	-

	Ru(101) Ru µg/g	Rh(103) Rh µg/g	Pd(105) Pd µg/g	Ag(107) Ag µg/g	Cd(111) Cd µg/g	In(115) In µg/g	Sn(118) Sn µg/g	Sb(121) Sb µg/g	Te(125) Te µg/g	Te(128) Te µg/g	Cs(133) Cs µg/g	Ba(135) Ba µg/g	Ba(137) Ba µg/g	Sm(147) Sm µg/g	Gd(157) Gd µg/g	Tb(159) Tb µg/g	Dy(163) Dy µg/g
barite line A (32µm, 2J/cm², 10Hz)	**b.d.l.**	**b.d.l.**	**n.d.**	**n.d.**	**b.d.l.**	**n.d.**	**b.d.l.**	**b.d.l.**	**b.d.l.**	**n.d.**	**0.3**	**599113**	**599290**	**n.d.**	**n.d.**	**n.d.**	**b.d.l.**
2RSD %	---	---	---	---	---	---	---	---	---	---	52	8	7	---	---	---	---
barite line B (32µm, 2J/cm², 10Hz)	**0.5**	**n.d.**	**n.d.**	**b.d.l.**	**n.d.**	**b.d.l.**	**b.d.l.**	**n.d.**	**n.d.**	**n.d.**	**0.3**	**585229**	**569107**	**n.d.**	**b.d.l.**	**n.d.**	**n.d.**
2RSD %	99	---	---	---	---	---	---	---	---	---	53	8	7	---	---	---	---
barite line C (32µm, 2J/cm², 10Hz)	**b.d.l.**	**b.d.l.**	**n.d.**	**n.d.**	**n.d.**	**b.d.l.**	**n.d.**	**b.d.l.**	**n.d.**	**n.d.**	**0.2**	**597056**	**574770**	**n.d.**	**b.d.l.**	**b.d.l.**	**b.d.l.**
2RSD %	---	---	---	---	---	---	---	---	---	---	56	8	7	---	---	---	---
barite line D (32µm, 2J/cm², 10Hz)	**n.d.**	**n.d.**	**b.d.l.**	**b.d.l.**	**b.d.l.**	**b.d.l.**	**0.2**	**b.d.l.**	**n.d.**	**n.d.**	**0.3**	**591014**	**571165**	**n.d.**	**n.d.**	**n.d.**	**b.d.l.**
2RSD %	---	---	---	---	---	---	93	---	---	---	40	8	7	---	---	---	---
barite line E (32µm, 2J/cm², 10Hz)	**b.d.l.**	**n.d.**	**n.d.**	**n.d.**	**n.d.**	**b.d.l.**	**b.d.l.**	**n.d.**	**b.d.l.**	**b.d.l.**	**0.4**	**587109**	**594443**	**0.3**	**b.d.l.**	**n.d.**	**b.d.l.**
2RSD %	---	---	---	---	---	---	---	---	---	---	48	8	7	65	---	---	---
barite line F (32µm, 2J/cm², 10Hz)	**b.d.l.**	**b.d.l.**	**n.d.**	**n.d.**	**b.d.l.**	**b.d.l.**	**n.d.**	**b.d.l.**	**n.d.**	**n.d.**	**0.5**	**594338**	**582290**	**n.d.**	**b.d.l.**	**n.d.**	**b.d.l.**
2RSD %	---	---	---	---	---	---	---	---	---	---	41	10	7	---	---	---	---
barite line G (32µm, 2J/cm², 10Hz)	**n.d.**	**n.d.**	**n.d.**	**n.d.**	**n.d.**	**n.d.**	**b.d.l.**	**n.d.**	**b.d.l.**	**b.d.l.**	**0.4**	**604267**	**594681**	**b.d.l.**	**n.d.**	**n.d.**	**b.d.l.**
2RSD %	---	---	---	---	---	---	---	---	---	---	41	8	7	---	---	---	---
barite line H (32µm, 2J/cm², 10Hz)	**n.d.**	**0.1**	**n.d.**	**b.d.l.**	**n.d.**	**n.d.**	**b.d.l.**	**n.d.**	**b.d.l.**	**2.6**	**0.4**	**595960**	**626983**	**n.d.**	**n.d.**	**n.d.**	**b.d.l.**
2RSD %	---	79	---	---	---	---	---	---	---	94	34	8	7	---	---	---	---
Standards	Ru µg/g	Rh µg/g	Pd µg/g	Ag µg/g	Cd µg/g	In µg/g	Sn µg/g	Sb µg/g	Te µg/g	Te µg/g	Cs µg/g	Ba µg/g	Ba µg/g	Sm µg/g	Gd µg/g	Tb µg/g	Dy µg/g
NIST612	n.d.	1	1	22	28	39	39	35	n.d.	n.d.	43	39	39	38	37	38	36
NIST610_611	n.d.	1	1	251	270	434	430	396	302	302	366	452	452	453	449	437	437
PGE_Ni7b	37	31.4	31.9	-	-	-	-	-	-	-	-	-	-	-	-	-	-

Table S3 (cont.):

	Ho(165) Ho µg/g	Er(166) Er µg/g	Tm(169) Tm µg/g	Yb(172) Yb µg/g	Lu(175) Lu µg/g	Ta(181) Ta µg/g	W(182) W µg/g	Re(185) Re µg/g	Os(189) Os, µg/g	Ir(193) Ir µg/g	Pt(195) Pt µg/g	Au(197) Au µg/g	Tl(205) Tl µg/g	Pb(208) Pb µg/g	Bi(209) Bi µg/g	Th(232) Th µg/g	U(238) U µg/g
barite line A (32µm, 2J/cm², 10Hz)	**b.d.l.**	**b.d.l.**	**n.d.**	**b.d.l.**	**0.0**	**b.d.l.**	**n.d.**	**b.d.l.**	**n.d.**	**b.d.l.**	**b.d.l.**	**b.d.l.**	**n.d.**	**3.1**	**b.d.l.**	**n.d.**	**b.d.l.**
2RSD %	---	---	---	---	71	---	---	---	---	---	---	---	---	32	---	---	---
barite line B (32µm, 2J/cm², 10Hz)	**b.d.l.**	**b.d.l.**	**b.d.l.**	**b.d.l.**	**0.1**	**n.d.**	**n.d.**	**n.d.**	**b.d.l.**	**b.d.l.**	**b.d.l.**	**b.d.l.**	**b.d.l.**	**8.0**	**n.d.**	**b.d.l.**	**b.d.l.**
2RSD %	---	---	---	---	72	---	---	---	---	---	---	---	---	28	---	---	---
barite line C (32µm, 2J/cm², 10Hz)	**b.d.l.**	**b.d.l.**	**n.d.**	**b.d.l.**	**0.0**	**n.d.**	**b.d.l.**	**b.d.l.**	**b.d.l.**	**b.d.l.**	**b.d.l.**	**b.d.l.**	**b.d.l.**	**1.9**	**b.d.l.**	**n.d.**	**n.d.**
2RSD %	---	---	---	---	98	---	---	---	---	---	---	---	---	31	---	---	---
barite line D (32µm, 2J/cm², 10Hz)	**b.d.l.**	**n.d.**	**n.d.**	**b.d.l.**	**n.d.**	**n.d.**	**n.d.**	**n.d.**	**b.d.l.**	**b.d.l.**	**b.d.l.**	**b.d.l.**	**n.d.**	**3.4**	**n.d.**	**b.d.l.**	**b.d.l.**
2RSD %	---	---	---	---	---	---	---	---	---	---	---	---	---	23	---	---	---
barite line E (32µm, 2J/cm², 10Hz)	**b.d.l.**	**b.d.l.**	**b.d.l.**	**n.d.**	**0.0**	**n.d.**	**n.d.**	**n.d.**	**n.d.**	**b.d.l.**	**n.d.**	**b.d.l.**	**n.d.**	**2.9**	**0.0**	**b.d.l.**	**0.0**
2RSD %	---	---	---	---	79	---	---	---	---	---	---	---	---	29	82	---	94
barite line F (32µm, 2J/cm², 10Hz)	**b.d.l.**	**b.d.l.**	**b.d.l.**	**b.d.l.**	**0.0**	**n.d.**	**b.d.l.**	**b.d.l.**	**n.d.**	**b.d.l.**	**b.d.l.**	**b.d.l.**	**b.d.l.**	**2.0**	**n.d.**	**n.d.**	**b.d.l.**
2RSD %	---	---	---	---	87	---	---	---	---	---	---	---	---	24	---	---	---
barite line G (32µm, 2J/cm², 10Hz)	**b.d.l.**	**n.d.**	**n.d.**	**n.d.**	**0.0**	**n.d.**	**n.d.**	**b.d.l.**	**b.d.l.**	**b.d.l.**	**b.d.l.**	**b.d.l.**	**b.d.l.**	**1.2**	**n.d.**	**n.d.**	**b.d.l.**
2RSD %	---	---	---	---	70	---	---	---	---	---	---	---	---	34	---	---	---
barite line H (32µm, 2J/cm², 10Hz)	**b.d.l.**	**b.d.l.**	**n.d.**	**b.d.l.**	**n.d.**	**b.d.l.**	**n.d.**	**b.d.l.**	**b.d.l.**	**b.d.l.**	**b.d.l.**	**b.d.l.**	**b.d.l.**	**1.6**	**b.d.l.**	**b.d.l.**	**b.d.l.**
2RSD %	---	---	---	---	---	---	---	---	---	---	---	---	---	33	---	---	---
Standards	Ho µg/g	Er µg/g	Tm µg/g	Yb µg/g	Lu µg/g	Ta µg/g	W µg/g	Re µg/g	Os, µg/g	Ir µg/g	Pt µg/g	Au µg/g	Tl µg/g	Pb µg/g	Bi µg/g	Th µg/g	U µg/g
NIST612	38	38	37	39	37	38	38	7	n.d.	0.0	3	5	15	39	30	38	37
NIST610_611	449	455	435	450	439	446	444	50	n.d.	n.d.	3	24	60	426	384	457	462
PGE_Ni7b	-	-	-	-	-	-	-	55	85	54	33	-	-	-	-	-	-

NIST SRM 610 and 612: Wise S.A., Watters R.L., National Institute of Standards and Technology, 2012, http://www.nist.gov/srm

PGE_Ni7b: pers. commun. Cora C. Wohlgemuth-Ueberwasser (see: DOI 10.1007/s00410-007-0212-x for details)

Strontium isotope laser ablation analysis

In-situ Sr isotope analyses including data reduction using the linear regression slope (LRS) method followed a previously published procedure initially developed for carbonates (Fietzke et al., 2008). For barite, the former method had to be modified slightly with respect to cup configuration and correction of isobaric interferences. The cup configuration used is provided in Table S4.

Table S4: Cup configuration for LA-MC-ICPMS Sr isotope analyses in barite samples. For all atomic mass units (amu) monitored the relative abundances (in %) of isotope of interest and isobaric interferences are provided.

Cup	amu	Sr	Kr	Rb	$BaAr^{2+}$	Er^{2+}	Yb^{2+}	Lu^{2+}	Hf^{2+}
L4	83		11.4953			33.61			
L3	83.5					22.93			
L2	85			72.1654	0.1058	14.93	3.04		
L1	86	9.8566	17.2984		0.1012		21.83		
AX	86.5						16.13		
H1	87	7.0015		27.8346	2.417		31.83		0.162

H2	87.5				6.592			97.416	
H3	88	82.5845			7.853		12.76	2.584	5.2604
H4	88.5				11.232				18.5953

In accordance with the results of elemental analyses using LA-ICPMS (Table S2) no significant contribution from doubly-charged REE ions could be found. The same is true for Hf, thus no correction for this group of elements was required.

Nevertheless, significant signal intensities on 87.5 amu and 88.5 amu occur during ablation of barite samples but are perfectly absent while ablating carbonates. Both contributions are strongly correlated (R^2=0.999995) yielding an 87.5/88.5 ratio of 0.5817 when evaluating all barite data. The latter observation points towards an interferences consisting of doubly-charged BaAr cluster ions (unfractionated ratio of $^{135}Ba^{40}Ar^{2+}/^{137}Ba^{40}Ar^{2+}$=0.5869). Based on the measured 88.5 intensity using the respective Ba isotope abundances, intensities measured on 86, 87 and 88 amu have been corrected for the contribution from $BaAr^{2+}$. For all barite samples this is by far the dominant interference correction. Changing Kr contributions to 86 amu had been monitored using 83 amu and were found to be insignificant. Due to the practical absence of Rb in the barite samples (see Table S2) the correction on 87 amu (^{87}Rb contribution) was also insignificant.

The reported $^{87}Sr/^{86}Sr$ results (Table 4) were calculated by applying the $BaAr^{2+}$ correction and the mass bias correction (exponential law; based on $^{86}Sr/^{88}Sr$=0.1194). The in-situ data are in good agreement with the bulk analyses $^{86}Sr/^{88}Sr$ results (Table 3), thus supporting the application of the $BaAr^{2+}$ correction.

Table S5: Fluid inclusion homogenization and trapping temperatures:

ALV2467-R2		ALV2464-R4		ALV2464-R4 (amorph. silica)	
$T_{Homogenization}$	$T_{Trapping}$	$T_{Homogenization}$	$T_{Trapping}$	$T_{Homogenization}$	$T_{Trapping}$
114	124	121	131	118	128
116	126	123	133	120	130
128	138	125	135	120	130
130	141	125	135	124	134
130	141	126	136	127	137
131	142	126	136		
133	144	126	136		
140	151	126	136		
147	158	133	144		
152	163	134	145		
155	166	135	146		
157	168	135	146		
160	172	135	146		
172	184	138	149		
173	185	142	153		
174	186	147	158		
174	186	161	173		
182	194	172	184		
183	195	173	185		
190	203	178	190		
195	208	183	195		
196	209	184	196		
196	209	191	204		
209	222	193	206		
214	227	216	229		
214	227	221	234		
218	231	222	235		
220	233	223	236		
229	242	223	236		
240	253	257	271		
243	256	266	280		
258	272	269	283		
Average	**181**		**189**		**132**
Std. Dev.	**47**		**41**		**4**